Higher-dimensional Jordan-Wigner transformation and auxiliary Majorana fermions

Kangle Li and Hoi Chun Po
Department of Physics, Hong Kong University of Science and Technology, Clear Water Bay, Hong Kong, China

(Received 28 September 2021; revised 12 May 2022; accepted 26 August 2022; published 8 September 2022)

We discuss a scheme for performing Jordan-Wigner transformation for various lattice fermion systems in two and three dimensions which keeps internal and spatial symmetries manifest. The correspondence between fermionic and bosonic operators is established with the help of auxiliary Majorana fermions. The current construction is applicable to general lattices with even coordination numbers and an arbitrary number of fermion flavors. The approach is demonstrated on the single-orbital square, triangular, and cubic lattices for spin-1/2 fermions. We also discuss the relation to some quantum spin liquid models.

DOI: 10.1103/PhysRevB.106.115109

I. INTRODUCTION

Bosonization has long been an important technique for describing and understanding many-body quantum systems. For instance, it allows one to directly apply tools developed for bosonic systems, like tensor network methods, to fermionic problems. Generally speaking, the fermionic statistics is implemented on the bosonic side using nonlocal string operators, as is well known in the classic Jordan-Wigner transformation for one-dimensional systems [1]. Generalizations of the transformation to higher dimensions using lattice gauge fields have also been proposed [2–24]. Such exact bosonization mappings are also important from the quantum simulation perspective, for they address the possibility of simulating a quantum many-body fermionic system using a bosonic quantum computer [25–30].

From a condensed matter physics perspective, it is natural to ask how symmetries on the fermionic side are represented on the bosonic side under the bosonization scheme. The symmetry aspect of bosonization, however, is rather subtle. For instance, although there is a clear physical distinction between a square and a triangular lattice, a bosonization scheme might effectively treat a triangular lattice simply as a sheared version of a square lattice and ignore the differences in their spatial symmetries [9]. Even if the bosonization transformation itself is exact, in practice any further attempt to solve the bosonized model typically invokes approximations. In the process, the symmetries which are nonmanifest on the bosonic side could be explicitly broken, and this could lead to misleading results.

In a recent work [31], we proposed an approach for performing higher-dimensional Jordan-Wigner transformation while keeping all symmetries manifest. The symmetry transformations on the bosonic side can all be traced down to that of a collection of operators denoted by $\Lambda^{\alpha x}$, which could be viewed as the bosonic analog (up to a Jordan-Wigner string) of the Majorana fermions defining the physical fermionic Hilbert space. The approach in Ref. [31], however, is limited to four-coordinated lattices like the two-dimensional (2D) square and three-dimensional (3D) diamond lattices with a single orbital per site. In this work, we generalize our construction to lattices with an even coordination number and an arbitrary number of orbitals. Our construction follows from decomposing $\Lambda^{\alpha x} = i\eta^{\alpha}\chi^{x}$ using auxiliary Majorana fermions η and χ. Here, the η fermions carry the physical quantum numbers and their bilinears generate internal symmetries. In contrast, the χ fermions encode the directional dependence in the bosonization scheme and their bilinears generate transformations which keep spatial symmetries manifest. Representing $\Lambda^{\alpha x}$ by some tensor products of Pauli matrices provides a qubit representation of the theory, in which every bilinear operator acts on the Hilbert space of some two-level bosonic degrees of freedom (e.g., spin-1/2), usually called "qubits." For simplicity, we will refer to this as the $\eta\chi$ approach henceforth.

The $\eta\chi$ approach discussed in the present work is inspired by earlier works providing lattice bosonization recipes through the introduction of Majorana fermions [7,9,27]. It is also closely related to the approach developed in Refs. [2,3,23,24], dubbed the "Γ model," given that the η and χ Majorana fermions provide a natural representation of the Clifford algebra. In particular, we emphasize that in the present bosonization scheme the number of auxiliary qubits depends only on the lattice fermionic model, and, at the same time, all internal and spatial symmetries relevant to the fermionic problem are kept manifest. This can be contrasted with some of the earlier works in which, for instance, the number of auxiliary qubits required grows as more electron hopping terms are considered on the fermionic model [7], or when the geometrical difference between, for instance, square and triangular lattices are ignored in the bosonization scheme [9]. Furthermore, in our approach internal symmetries, which act in an on-site manner on the fermionic side, will continue to act on site on the bosonic side. We also allow for an arbitrary number of complex fermionic modes on each site and incorporate naturally any possible internal symmetries among the fermion flavors, although we will limit the majority of our discussion to lattices with even coordination numbers.

The paper is organized as follows: We introduce the general procedures of our bosonization scheme in Sec. II. We define the operators invoked and discuss the fermion-boson mapping as well as the constraints of the bosonized problem. The general procedure is then demonstrated on three successively more complicated lattices in Secs. III–V, in which we derive the explicit representations for their associated spatial symmetries. As a warmup, we revisit the bosonization problem on the square lattice in Sec. III within the $\eta\chi$ formalism. We review the constraints defining the fermionic states within the bosonic Hilbert space, and also discuss how the spatial symmetries are implemented. In Sec. IV we provide a parallel discussion for the triangular lattice, which is six coordinated and goes beyond the approach developed in Ref. [31]. In Sec. V, we further apply the $\eta\chi$ formalism to the 3D cubic lattice, which is also six coordinated. The operator constraints defining the fermionic subspace are more complicated in three dimensions, and we provide a strategy for finding independent constraints. We also analyze in detail how symmetries are implemented on the bosonized model, and discuss how fermion-odd operators can also be identified on the bosonic side [31]. Next, as a demonstration on how our approach could aid the design of spin liquid models respecting the symmetries of the underlying lattice, in Sec. VI we consider the bosonization of a chiral p-wave superconductor on the triangular lattice. The bosonization gives a chiral spin liquid model defined on a triangular lattice with three qubits per site. Such models could be relevant to the correlated electronic problem in moiré heterostructures [32–37]. We then conclude in Sec. VII with a discussion on how the $\eta\chi$ formalism might be generalized to odd-coordinated systems, and elaborate on the relations of our approach with the design of exactly solved quantum spin liquid models [38–40].

II. GENERAL PROCEDURES

A. One-dimensional Jordan-Wigner transformation

To begin with, let us review the basic idea of one-dimensional Jordan-Wigner transformation. For a one-dimensional finite chain of complex fermions, we first decompose complex fermion creation and annihilation operators into Majorana fermions, i.e., $c_x = \frac{1}{2}(\gamma_x^1 + i\gamma_x^2)$ on the site x. Operators γ_1^i, $i = 1, 2$, on a single site, say, the left end of the chain, form a Clifford algebra, and we can use Pauli matrices to represent them, thus obtaining a qubit description. Furthermore, two Majorana operators $\gamma_x^i, \gamma_{x'}^j$ on two different sites anticommute with each other, and so to retain the anticommutation relations one introduces nonlocal Pauli strings in the representation of γ_x^i, $x > 1$. Formally, we can map

$$\begin{aligned} \gamma_1^1 &\longmapsto X_1, \quad \gamma_1^2 \longmapsto Y_1, \\ \gamma_2^1 &\longmapsto Z_1X_2, \quad \gamma_2^2 \longmapsto Z_1Y_2, \\ &\vdots \\ \gamma_x^1 &\longmapsto \left(\prod_{l<x} Z_l\right)X_x, \quad \gamma_x^2 \longmapsto \left(\prod_{l<x} Z_l\right)Y_x. \end{aligned} \tag{1}$$

One can check that these bosonized operators obey the same (anti)commutation relations as the original Majorana operators. For a fermion-even operator like the bilinear form $i\gamma_x^1\gamma_{x+1}^2$, the long product of Z_l operators cancels and so the bilinear form still maps to a local operator Y_xY_{x+1}. After bosonization, we can focus on the bosonic Hilbert space of a spin-1/2 chain. For example, consider the Kitaev chain model with Hamiltonian

$$H_K = -\sum_{x=1}^{N} i\gamma_x^1\gamma_{x+1}^2 \longmapsto H_I = -\sum_{x=1}^{N} Y_xY_{x+1}, \tag{2}$$

where the bosonized Hamiltonian is an Ising model.

If we turn to higher dimensions, similar construction can still be employed provided that one prescribes a one-dimensional ordering of the sites along which the Pauli string is introduced. For a generic fermionic model, the Pauli string no longer cancels after bosonization. Thus the locality of the operators is not well preserved. The goal of constructing a higher-dimensional Jordan-Wigner transformation is to overcome such nonlocality problems in applying the original approach to higher dimensions. We will next discuss how this could be achieved by introducing auxiliary Majorana fermionic partons for each bond of the lattice, followed by suitable constraints on the parton Hilbert space.

B. Higher-dimensional constructions

Consider an arbitrary lattice fermionic system, which can be viewed as a connected graph consisting of some vertices and edges. We first consider the operators localized to each site $\boldsymbol{r}$. Suppose we have m complex fermionic modes, $f_{\boldsymbol{r}}^1, f_{\boldsymbol{r}}^2, \ldots, f_{\boldsymbol{r}}^m$. We can represent them by $2m$ Majorana operators $\gamma_{\boldsymbol{r}}^k$, $k = 1, 2, \ldots, 2m$, through

$$f_{\boldsymbol{r}}^n = \tfrac{1}{2}\left(\gamma_{\boldsymbol{r}}^{2n-1} - i\gamma_{\boldsymbol{r}}^{2n}\right), \quad f_{\boldsymbol{r}}^{n\dagger} = \tfrac{1}{2}\left(\gamma_{\boldsymbol{r}}^{2n-1} + i\gamma_{\boldsymbol{r}}^{2n}\right), \tag{3}$$

for $1 \leqslant n \leqslant m$. These Majorana fermions obey anticommutation relations

$$\left\{\gamma_{\boldsymbol{r}}^i, \gamma_{\boldsymbol{r}'}^j\right\} = 2\delta^{ij}\delta_{\boldsymbol{r}\boldsymbol{r}'}. \tag{4}$$

All operators in fermions f^i can be rewritten in terms of γ^i. In particular, terms in the Hamiltonian can always be written as sum and product of the bilinears $i\gamma_{\boldsymbol{r}}^i\gamma_{\boldsymbol{r}'}^j$. Similar to Pauli operators in the one-dimensional case, we want to construct local bosonic operators (which we call $\Theta_{\boldsymbol{r}}$ and $\Lambda_{\boldsymbol{r}}$) such that all bilinear forms can be represented as products of them. Then the local bosonic Hilbert space can be constructed from qubit representations of these local bosonic operators.

The $\eta\chi$ formalism provides a defining representation of desired bosonic operators $\Theta_{\boldsymbol{r}}, \Lambda_{\boldsymbol{r}}$. It encodes the fermionic problem in a bosonic Hilbert space as follows. To each site, we attach Majorana operators $\eta_{\boldsymbol{r}}^\alpha$, $\alpha \in \{1, 2, \ldots, 2m\}$, and $\chi_{\boldsymbol{r}}^x$, $x \in \{1, 2, \ldots, n_{\boldsymbol{r}}\}$, where $n_{\boldsymbol{r}}$ is the coordination number of the site (for the examples we study in the following, $n_{\boldsymbol{r}}$ is a global constant independent of $\boldsymbol{r}$). We assume $n_{\boldsymbol{r}}$ is even for all $\boldsymbol{r}$, and set $n_{\boldsymbol{r}} = 2n$; i.e., we further restrict ourselves to even-coordinated lattices. Then we define operators

$$\Theta_{\boldsymbol{r}}^{\alpha\beta} = i\eta_{\boldsymbol{r}}^\alpha\eta_{\boldsymbol{r}}^\beta, \quad \Lambda_{\boldsymbol{r}}^{\alpha x} = i\eta_{\boldsymbol{r}}^\alpha\chi_{\boldsymbol{r}}^x, \quad \Phi_{\boldsymbol{r}}^{xy} = -i\chi_{\boldsymbol{r}}^x\chi_{\boldsymbol{r}}^y. \tag{5}$$

From these expressions one can readily check that Θ, Λ, and Φ satisfy the relations in Ref. [31],

$$\Lambda_{\boldsymbol{r}}^{\alpha x} = -i\Theta_{\boldsymbol{r}}^{\alpha\beta}\Lambda_{\boldsymbol{r}}^{\beta x}, \quad \Phi_{\boldsymbol{r}}^{xy} = -\Lambda_{\boldsymbol{r}}^{\alpha x}\Theta_{\boldsymbol{r}}^{\alpha\beta}\Lambda_{\boldsymbol{r}}^{\beta y}, \tag{6}$$

where there is no summation on the repeated indices. Both $\Theta_{\boldsymbol{r}}^{\alpha\beta}$ and $\Lambda_{\boldsymbol{r}}^{\alpha x}$ are Hermitian, and meanwhile both $\Theta_{\boldsymbol{r}}^{\alpha\beta}$ and $\Phi_{\boldsymbol{r}}^{xy}$ are antisymmetric in their upper indices. Note that although $\Lambda^{\alpha x}$ is a 4×4 operator-valued matrix in Ref. [31], in the current approach it can be an even-by-even rectangular matrix in general.

Fermion bilinears in the physical problem can be mapped to the bosonic operators Θ and Λ through

$$\begin{aligned} i\gamma_{\boldsymbol{r}}^{\alpha}\gamma_{\boldsymbol{r}}^{\beta} &\to \Theta_{\boldsymbol{r}}^{\alpha\beta}, \\ i\gamma_{\boldsymbol{r}}^{\alpha}\gamma_{\boldsymbol{r}'}^{\beta} &\to \Lambda_{\boldsymbol{r}}^{\alpha x}\Lambda_{\boldsymbol{r}'}^{\beta y}, \end{aligned} \tag{7}$$

where $\boldsymbol{r}$ and $\boldsymbol{r}'$ are the ending and starting sites of a given arrow (an oriented edge) in the lattice. If this orientation is reversed on the left-hand side, then there is an extra minus sign on the right-hand side. Here, x, y are numbers labeling the Majorana $\chi^{x,y}$ at two ends of the edge. We also demand $\Theta^{\alpha\beta}$ and $\Lambda^{\alpha x}$ satisfy the same commutation and anticommutation relations as the fermion bilinears they represent: the two operators $\Theta^{\alpha\beta}$ and $\Lambda^{\alpha' x}$ anticommute if and only if α' is equal to either α or β; otherwise, they commute. Similarly, the two operators Φ^{xy} and $\Lambda^{\alpha z}$ anticommute if z is equal to x or y, and commute otherwise. The two operators $\Theta^{\alpha\beta}$ and Φ^{xy} always commute. For applications we will also discuss qubit representations of $\Theta^{\alpha\beta}$ and $\Lambda^{\alpha x}$ in following sections.

In this construction, $\eta^{\alpha'}$s correspond to physical degrees of freedom, while $\chi^{x'}$s are auxiliary Majorana fermions connecting different sites. We often call them Majorana *partons*. The number of $\eta^{\alpha'}$s and the number of $\chi^{x'}$s are not necessarily the same. This is different from the formalism in Ref. [31], which relied on an exceptional isomorphism of the group Spin(4). The internal symmetries like fermion parity, time reversal, and flavor symmetries are characterized by transformations of $\eta^{\alpha'}$s. Spatial symmetries, like translation, reflection, and rotation, are characterized by transformations of $\chi^{x'}$s.

To be more explicit, let us take a closer look at the transformations of $\Lambda^{\alpha x} = i\eta^{\alpha}\chi^{x}$. The bilinear operators $\theta^{\alpha\beta} = \frac{i}{2}\eta^{\alpha}\eta^{\beta}$ form a set of generators of $\mathfrak{so}(2m)$ algebra:

$$[\theta^{\alpha\beta}, \theta^{\rho\lambda}] = i(\delta^{\alpha\lambda}\theta^{\beta\rho} + \delta^{\beta\rho}\theta^{\alpha\lambda} - \delta^{\alpha\rho}\theta^{\beta\lambda} - \delta^{\beta\lambda}\theta^{\alpha\rho}). \tag{8}$$

The exponentiation of elements in the algebra form the Spin($2m$) group which is the double cover of SO($2m$). A similar structure can be introduced for $\phi_{\boldsymbol{r}}^{xy} = -\frac{i}{2}\chi^{x}\chi^{y}$ which form a set of generators of $\mathfrak{so}(2n)$ algebra. Furthermore, we have

$$[\theta^{\alpha\beta}, \eta^{\lambda}] = i(\delta^{\beta\lambda}\eta^{\alpha} - \delta^{\alpha\lambda}\eta^{\beta}), \quad \alpha \neq \beta. \tag{9}$$

An element in Spin($2m$) can be written as $U(A) = e^{-i\sum_{\alpha\beta}A_{\alpha\beta}\theta^{\alpha\beta}}$, where A is a $2m\times 2m$ real antisymmetric matrix. Using Eq. (9), we see

$$U(A)\eta^{\lambda}U(A)^{-1} = \sum_{\lambda'}\left(e^{-2A}\right)_{\lambda\lambda'}\eta^{\lambda'}. \tag{10}$$

The matrix e^{-2A} is an element in SO($2m$), meaning η^{k} transforms as an SO($2m$) vector. Similarly we define $V(A) = e^{-i\sum_{xy}A_{xy}\phi^{xy}}$. χ^{x} transforms as an SO($2n$) vector. Combining these properties, $\Lambda^{\lambda x} = i\eta^{\lambda}\chi^{x}$ will transform as an SO($2m$) vector in its first index and as an SO($2n$) vector in its second index independently:

$$\begin{aligned} U(A)\Lambda^{\alpha x}U(A)^{-1} &= \sum_{\alpha'}(e^{-2A})_{\alpha\alpha'}\Lambda^{\alpha' x}, \\ V(A)\Lambda^{\alpha x}V(A)^{-1} &= \sum_{x'}\Lambda^{\alpha x'}(e^{-2A})_{x'x}. \end{aligned} \tag{11}$$

So to find transformations among different $\chi^{x'}$s or $\eta^{\alpha'}$s, we only need to find some suitable matrix A. This allows one to systematically identify symmetry operations on the bosonic side [31]. In Secs. III and IV we will discuss symmetry transformations in explicit examples.

C. Enlarged Hilbert space and constraints

We have seen the mapping from a fermion problem to a bosonic system, where auxiliary Majorana partons are introduced to intermediate operators supported on multiple sites. These partons will make the bosonic Hilbert space larger than the original fermionic Hilbert space. For example, when the original fermion problem is in a lattice of coordination number 4, and has a spinful fermion per site, then the bosonized system will have four extra Majorana partons; thus the bosonized on-site Hilbert space is enlarged to $2^{2+2} = 16$ dimensions. To return to the same dimension of fermionic Hilbert space, we have to impose 2^2 constraints per site. Generically we argue that after imposing suitable constraints the bosonized system has the same dimension of Hilbert space as that of the fermion problem. Examples are presented in Secs. III–V and Appendix B.

First we consider parton parity $\Gamma_{\boldsymbol{r}} \propto \eta_{\boldsymbol{r}}^{1}\eta_{\boldsymbol{r}}^{2}\cdots\ \chi_{\boldsymbol{r}}^{1}\chi_{\boldsymbol{r}}^{2}\cdots$ on each site. Fixing $\Gamma_{\boldsymbol{r}}$ to be a constant can reduce the enlarged Hilbert space by one dimension. If we denote the total number of sites by N, then we have N constraints. There is some flexibility of choosing the parity to be even or odd, but we can always make these on-site partons translationally invariant to simplify the bosonized problem.

A second type of constraint comes from the identities in the original fermion problem. Because of the relation $(\gamma_{\boldsymbol{r}}^{i})^2 = 1$, the product of a loop of $(\gamma_{\boldsymbol{r}}^{i})^2_{\boldsymbol{r}\in\text{a loop}}$ is also identity. This becomes a nontrivial constraint after mapping to the bosonized problem. Each such constraint will also reduce the enlarged Hilbert space by one dimension. So we only need to count the independent constraints in the lattice. This is equivalent to counting the independent cycles in the lattice.

A systematic way of doing this is to treat the lattice as a graph consisting of vertices and edges. We should choose a set of generators of the free Abelian group H_1, which is the first homology group of the graph. For a generic connected graph X, the first homology group can be found with the notion *maximal tree* [41]. A tree is defined as a connected subgraph with no loops, and a maximal tree T is a tree which contains all vertices of X. We denote the sets of edges and vertices of a system as $E(X)$ and $V(X)$, respectively. For a concrete example see Fig. 8, in which there are 15 edges and 9 vertices. The number of edges in a maximal tree is $|E(T)| = |V(X)| - 1$, where "$|\cdot|$" means the number of elements in a set [42]. Then every edge which is not contained in the maximal tree will be a generator of homology class in $H_1(X)$. Note that different choices of maximal trees will give the same homology group.

The first homology group is

$$H_1(X) \cong \mathbb{Z}^{|E(X)|-|E(T)|} = \mathbb{Z}^{|E(X)|-|V(X)|+1}. \tag{12}$$

In particular, for a planar graph, the number $(|E(X)| - |E(T)|)$ is equal to the number of "holes" in the graph. For nonplanar graphs, like embedding on a closed manifold, the choices of generators will be more complicated and depend on the details of the graph. In our following examples, this counting includes both plaquette constraints and large Wilson loop constraints.

We stress that the discussion above is in general applicable for an arbitrary lattice system in which every vertex has an even coordination number. We can count the degrees of freedom and the number of independent constraints for a given graph X. For instance, we have $\eta_{\boldsymbol{r}}^{\alpha}$, $\alpha \in \{1, 2, \ldots, 2m_{\boldsymbol{r}}\}$, $\chi_{\boldsymbol{r}}^{x}$, $x \in \{1, 2, \ldots, n_{\boldsymbol{r}}\}$. The coordination number $n_{\boldsymbol{r}}$ is the number of edges linking to site $\boldsymbol{r}$. Notice that $|E(X)| = \sum_{\boldsymbol{r}} n_{\boldsymbol{r}}/2$, so combining the on-site parton parity projection and plaquette constraints we obtain

$$\begin{aligned}\dim\mathcal{H}_X &= \frac{\prod_{\boldsymbol{r}} 2^{m_{\boldsymbol{r}}} 2^{n_{\boldsymbol{r}}/2}}{2^{|V(X)|} 2^{|E(X)|-|V(X)|+1}} \\ &= \frac{2^{|E(X)|} \prod_{\boldsymbol{r}} 2^{m_{\boldsymbol{r}}}}{2^{|E(X)|+1}} \\ &= \frac{1}{2} \prod_{\boldsymbol{r}} 2^{m_{\boldsymbol{r}}},\end{aligned} \tag{13}$$

where the factor 1/2 shows the feature of a half Hilbert space with certain global fermionic parity. For lattices with odd coordination numbers, the above counting is still applicable, but then it is more subtle since to construct a local Hilbert space we should have even numbers of Majorana fermions. We discuss these issues in Sec. VII.

III. MAJORANA REPRESENTATION FOR SQUARE LATTICE

In this section, we study the example of a square lattice. After introducing the operators involved, we will discuss how to express the states in terms of qubits. We also discuss some issues pertaining to the global properties of the transformation, e.g., issues of putting the system on a torus. We also show the effect of locally relabeling the Majorana partons and rotational transformations explicitly.

Let us focus on the case of spin-1/2 fermions and a single orbital per site. On each site the Hilbert space is four dimensional, spanned by the basis $\{|0\rangle, f_{\uparrow}^{\dagger}|0\rangle, f_{\downarrow}^{\dagger}|0\rangle, f_{\uparrow}^{\dagger}f_{\downarrow}^{\dagger}|0\rangle\}$. Generically the Hamiltonian of the system can be built from quadratic forms of fermionic creation and annihilation operators. In particular, the products of quadratic forms compose interaction terms. So we mainly focus on quadratic terms. Let γ^i, $i = 1, 2, 3, 4$, be on-site Majorana operators such that

$$\begin{aligned} f_{\uparrow} &= \tfrac{1}{2}(\gamma^1 - i\gamma^2), \quad f_{\uparrow}^{\dagger} = \tfrac{1}{2}(\gamma^1 + i\gamma^2), \\ f_{\downarrow} &= \tfrac{1}{2}(\gamma^3 - i\gamma^4), \quad f_{\downarrow}^{\dagger} = \tfrac{1}{2}(\gamma^3 + i\gamma^4). \end{aligned} \tag{14}$$

For simplicity we choose arrow directions to be antiparallel to directions of basis vectors $\boldsymbol{x}, \boldsymbol{y}$, as shown in Fig. 1. Then by the definition in Eq. (5) and the mapping in Eq. (6) we obtain $\Theta^{\alpha\beta}$, $\Lambda^{\alpha x}$, $\Phi^{x,y}$, $\alpha, \beta, x, y \in \{1, 2, 3, 4\}$.

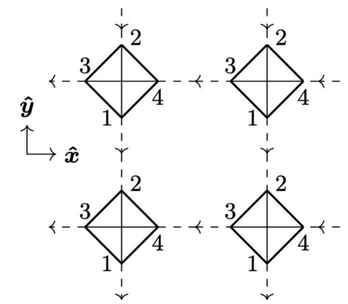

FIG. 1. The auxiliary Majorana fermions of a square lattice. Each site has a tilted square, with every vertex index $w \in \{1, 2, 3, 4\}$ representing $\chi_{\boldsymbol{r}}^{w}$. Each dashed line connects two sites, and its arrow tells how to determine the sign of an intersite product $i\chi_{\boldsymbol{r}}^{w}\chi_{\boldsymbol{r}'}^{w'}$.

We can study some examples to better reveal the meaning of the $\Theta_{\boldsymbol{r}}$ and $\Lambda_{\boldsymbol{r}}$ operators. First, consider the on-site particle number operator for spin up (and similarly for spin down),

$$n_{\uparrow} = f_{\uparrow}^{\dagger}f_{\uparrow} = \frac{1 + i\gamma^2\gamma^1}{2} \rightarrow \frac{1 + \Theta_{\boldsymbol{r}}^{21}}{2}. \tag{15}$$

If we replace Θ^{21} by its η representation, then it turns out that η^i has a similar physical meaning with γ^i. In other words, if we recombine η's again into complex fermionic partons, say,

$$\begin{aligned} \eta^1 &= a + a^{\dagger}, \quad \eta^2 = i(a - a^{\dagger}), \\ \eta^3 &= b + b^{\dagger}, \quad \eta^4 = i(b - b^{\dagger}), \end{aligned} \tag{16}$$

then $a^{\dagger}a$ and $b^{\dagger}b$ correspond to the number of spin-up and spin-down particles, respectively. We remark that although such equivalence is evident from the perspective of the on-site operators, $\eta_{\boldsymbol{r}}^{\alpha}$ is nevertheless different from $\gamma_{\boldsymbol{r}}^{\alpha}$ since $\gamma_{\boldsymbol{r}}^{\alpha}\gamma_{\boldsymbol{r}'}^{\beta} \neq \eta_{\boldsymbol{r}}^{\alpha}\eta_{\boldsymbol{r}'}^{\beta}$. This is where $\chi_{\boldsymbol{r}}^{x}$ plays a crucial role—to connect different sites. Actually, the parton construction of Θ and Λ could be done in a different way. For these spinful fermions on a square lattice, the Lie algebra formed by $\Theta^{\alpha\beta}$ has an equivalence $\mathfrak{so}(4) \cong \mathfrak{su}(2) \oplus \mathfrak{su}(2)$; on the Lie group level it is $\mathrm{Spin}(4) \cong \mathrm{SU}(2) \times \mathrm{SU}(2)$. Using this, one can separate charge and spin degrees of freedom in the parton description. In that construction the correspondence with the physical fermions will not be as simple [31].

We further introduce complex fermionic partons for χ,

$$\begin{aligned} \chi^1 &= d + d^{\dagger}, \quad \chi^2 = i(d - d^{\dagger}), \\ \chi^3 &= g + g^{\dagger}, \quad \chi^4 = i(g - g^{\dagger}). \end{aligned} \tag{17}$$

Auxiliary fermion modes $d^{\dagger}$ and $g^{\dagger}$ enlarge the Hilbert space of a single site to be 16 dimensional. To obtain the correct physical Hilbert space we need some extra reductions. The discussion in Ref. [31] requires the parton parity on site to be frozen at -1, but such a constraint is not present here. Nevertheless, as the bosonized Hamiltonian is built using the Θ, Λ, and Φ operators, which are all bilinears in η and χ, the on-site parity operator for any site commutes with the bosonized Hamiltonian. In other words, we can project to a particular sector of on-site parton parity operator to obtain a bosonic model, i.e.,

$$\Gamma_{\boldsymbol{r}} \equiv i^4 \eta_{\boldsymbol{r}}^1 \eta_{\boldsymbol{r}}^2 \eta_{\boldsymbol{r}}^3 \eta_{\boldsymbol{r}}^4 \chi_{\boldsymbol{r}}^1 \chi_{\boldsymbol{r}}^2 \chi_{\boldsymbol{r}}^3 \chi_{\boldsymbol{r}}^4 \overset{c}{=} \rho, \tag{18}$$

where $\rho \in \{+1, -1\}$ is a constant which we take to be $\boldsymbol{r}$ independent, and "$\overset{c}{=}$" means that the equality holds in the constrained Hilbert space. This is because $\Gamma_{\boldsymbol{r}}$ is the local fermion parity of the enlarged Hilbert space. To maintain the possible translation invariance of the states, it is natural to project to the subspace of the same parton parity everywhere.

A. Qubit representation

The on-site Hilbert space in the $\eta\chi$ description is generated by acting creation operators $a^\dagger$, $b^\dagger$, $d^\dagger$, and $g^\dagger$ on the vacuum. We can introduce some qubits for each site, and identify an unoccupied state $|0\rangle$ with $|\uparrow\rangle$ and an occupied state $|1\rangle$ with $|\downarrow\rangle$; then the Hilbert space can be represented by four qubits. Let the base states be defined as

$$|n_a n_b n_d n_g\rangle = (a^\dagger)^{n_a}(b^\dagger)^{n_b}(d^\dagger)^{n_d}(g^\dagger)^{n_g}|0\rangle. \tag{19}$$

They correspond to a four-qubit basis naturally; for instance,

$$|1000\rangle = |{\downarrow\uparrow\uparrow\uparrow}\rangle, \quad |0110\rangle = |{\uparrow\downarrow\downarrow\uparrow}\rangle.$$

The actions of $\Theta_{\boldsymbol{r}}$, $\Lambda_{\boldsymbol{r}}$, and $\Phi_{\boldsymbol{r}}$ on the Hilbert space can be represented as strings of Pauli matrices and identity operator, $\{\mathbb{1}, X, Y, Z\}$. For instance,

$$\Theta^{12} = i^2(a + a^\dagger)(a - a^\dagger) = (1 - 2n_a) = Z^{(1)}, \tag{20}$$

where the superscript "1" refers to the first qubit. The equality holds in the sense of acting on quantum states. The operators in qubit representation are as follows:

$$\begin{aligned}
&\Theta^{12} = Z^{(1)}, \Theta^{34} = Z^{(2)},\\
&\Theta^{13} = Y^{(1)}X^{(2)}, \Theta^{24} = -X^{(1)}Y^{(2)},\\
&\Theta^{14} = -Y^{(1)}Y^{(2)}, \Theta^{23} = X^{(1)}X^{(2)},
\end{aligned} \tag{21a}$$

$$\begin{aligned}
&\Lambda^{11} = Y^{(1)}Z^{(2)}X^{(3)}, \Lambda^{22} = -X^{(1)}Z^{(2)}Y^{(3)},\\
&\Lambda^{33} = Y^{(2)}Z^{(3)}X^{(4)}, \Lambda^{44} = -X^{(2)}Z^{(3)}Y^{(4)},
\end{aligned} \tag{21b}$$

$$\begin{aligned}
&\Phi^{12} = -Z^{(3)}, \Phi^{34} = -Z^{(4)},\\
&\Phi^{13} = -Y^{(3)}X^{(4)}, \Phi^{24} = X^{(3)}Y^{(4)},\\
&\Phi^{14} = Y^{(3)}Y^{(4)}, \Phi^{23} = -X^{(3)}X^{(4)}.
\end{aligned} \tag{21c}$$

We can, however, impose the projection $\Gamma_{\boldsymbol{r}} = Z_{\boldsymbol{r}}^{(1)}Z_{\boldsymbol{r}}^{(2)}Z_{\boldsymbol{r}}^{(3)}Z_{\boldsymbol{r}}^{(4)} \overset{c}{=} \rho$ to reduce the degrees of freedom by half. Equivalently, the last qubit $Z^{(4)}$ is in fact fully determined by the other three qubits. We can therefore obtain a more efficient description using only the first three qubits, with the state in the last qubit understood to be constrained by that of the first three. This way, we can simply replace the Pauli operators on the fourth qubit by the coefficient they generate, i.e.,

$$\begin{aligned}
&X^{(4)} \Rightarrow \mathbb{1},\\
&Z^{(4)} \Rightarrow \rho Z^{(1)}Z^{(2)}Z^{(3)},\\
&Y^{(4)} \Rightarrow i\rho Z^{(1)}Z^{(2)}Z^{(3)}.
\end{aligned} \tag{22}$$

The last line can also be obtained from $Y^{(4)} = iX^{(4)}Z^{(4)}$. By these replacements, the last qubit is "hidden" while the possible coefficients from actions on the last qubit are absorbed into operators acting on other qubits. Then $\Lambda^{\alpha x}$ is a 4×4 operator-valued matrix

$$\Lambda^{\alpha x} = \begin{pmatrix} Y^{(1)}Z^{(2)}X^{(3)} & -Y^{(1)}Z^{(2)}Y^{(3)} & Y^{(1)}Z^{(2)}Z^{(3)} & \rho X^{(1)} \\ X^{(1)}Z^{(2)}X^{(3)} & -X^{(1)}Z^{(2)}Y^{(3)} & X^{(1)}Z^{(2)}Z^{(3)} & -\rho Y^{(1)} \\ Y^{(2)}X^{(3)} & -Y^{(2)}Y^{(3)} & Y^{(2)}Z^{(3)} & \rho Z^{(1)}X^{(2)} \\ X^{(2)}X^{(3)} & -X^{(2)}Y^{(3)} & X^{(2)}Z^{(3)} & -\rho Z^{(1)}Y^{(2)} \end{pmatrix}_{\alpha x}. \tag{23}$$

Compared to fermionic Hilbert space, we have an extra qubit as an auxiliary degree of freedom. This unphysical degree of freedom is consumed when we consider the mapping of an identity from the fermionic side:

$$\begin{aligned}
1 &= \left(i\gamma_{\boldsymbol{r}}^2\gamma_{\boldsymbol{r}}^4\right)\left(i\gamma_{\boldsymbol{r}}^4\gamma_{\boldsymbol{r}+x}^3\right)\left(i\gamma_{\boldsymbol{r}+x}^3\gamma_{\boldsymbol{r}+x}^2\right)\left(i\gamma_{\boldsymbol{r}+x}^2\gamma_{\boldsymbol{r}+x+y}^1\right)\\
&\quad\times \left(i\gamma_{\boldsymbol{r}+x+y}^1\gamma_{\boldsymbol{r}+x+y}^3\right)\left(i\gamma_{\boldsymbol{r}+x+y}^3\gamma_{\boldsymbol{r}+y}^4\right)\left(i\gamma_{\boldsymbol{r}+y}^4\gamma_{\boldsymbol{r}+y}^1\right)\left(i\gamma_{\boldsymbol{r}+y}^1\gamma_{\boldsymbol{r}}^2\right)\\
\to 1 &= \Theta_{\boldsymbol{r}}^{24}\Lambda_{\boldsymbol{r}}^{44}\Lambda_{\boldsymbol{r}+x}^{33}\Theta_{\boldsymbol{r}+x}^{32}\Lambda_{\boldsymbol{r}+x}^{22}\Lambda_{\boldsymbol{r}+x+y}^{11}\Theta_{\boldsymbol{r}+x+y}^{13}\\
&\quad\times \Lambda_{\boldsymbol{r}+x+y}^{33}\Lambda_{\boldsymbol{r}+y}^{44}\Theta_{\boldsymbol{r}+y}^{41}\Lambda_{\boldsymbol{r}+y}^{11}\Lambda_{\boldsymbol{r}}^{22}\\
&\Rightarrow \hat{C}_{\boldsymbol{r}} \equiv \Phi_{\boldsymbol{r}}^{24}\Phi_{\boldsymbol{r}+x}^{32}\Phi_{\boldsymbol{r}+x+y}^{13}\Phi_{\boldsymbol{r}+y}^{41} \overset{c}{=} -1.
\end{aligned} \tag{24}$$

The minus sign in the last line is due to the anticommuting property of $\Theta_{\boldsymbol{r}}^{24}$ and $\Lambda_{\boldsymbol{r}}^{22}$, as we move $\Lambda_{\boldsymbol{r}}^{22}$ to the left end. As discussed above, Majorana operators χ^x are auxiliary and "unphysical," so $\Phi^{xy'}$s as bilinears of auxiliary operators somehow play the role of "gauge operators." Equation (24) is a constraint such that auxiliary degrees of freedom are restricted to be consistent with the fermion identity on the first line. For each plaquette there is a constraint equation, so effectively there is one independent constraint for each site and thus the on-site Hilbert space of the system is reduced to four dimensions. By degree counting, all extra degrees of freedom are killed by the parton parity constraint $\Gamma_{\boldsymbol{r}}$ and this plaquette constraint, so there are no other independent constraints.

In the qubit representation, by exploiting expressions of Φ^{xy} the constraint can be shown as

$$Y_{\boldsymbol{r}}^{(3)}X_{\boldsymbol{r}+x}^{(3)}Y_{\boldsymbol{r}+x+y}^{(3)}X_{\boldsymbol{r}+y}^{(3)} = (Z^{(1)}Z^{(2)})_{\boldsymbol{r}}(Z^{(1)}Z^{(2)})_{\boldsymbol{r}+y}. \tag{25}$$

The left-hand side of the constraint is the Hamiltonian in Wen's plaquette model [43], which is known to be equivalent to the toric code model [44] and describes the $\mathbb{Z}_2$ topological order. In the work of Chen *et al.* such constraints are interpreted as flux attachments of gauge fields [20–22]. In our construction, the left-hand side is not fixed but depends on values of physical degrees of freedom. These independent plaquette constraints can be implemented in the Hamiltonian as a summation $K\sum_{\boldsymbol{r}}\hat{C}_{\boldsymbol{r}}$ with coupling K sufficiently large so that the $\hat{C}_{\boldsymbol{r}}$ are enforced to be -1.

B. Wilson loops and fermion-odd operators

If we put the lattice system of N sites on a torus manifold, i.e., with periodic boundary conditions, then only $N-1$ plaquette constraints will be independent since the product of all plaquette operators $C_{\boldsymbol{r}}$ is the identity operator on the bosonic side by definition (5). Moreover, there will be extra global constraints from Wilson loops. To see this, let the lattice size be $L_x \times L_y$ and $r_{x,y} \in \mathbb{Z}/(L_{x,y}\mathbb{Z})$. From the fermionic side, there is an identity for products of Majorana operators along a y loop,

$$\left(i\gamma_{\boldsymbol{r}}^1\gamma_{\boldsymbol{r}}^2\right)\left(i\gamma_{\boldsymbol{r}}^2\gamma_{\boldsymbol{r}+\boldsymbol{y}}^1\right)\cdots\left(i\gamma_{\boldsymbol{r}-\boldsymbol{y}}^2\gamma_{\boldsymbol{r}}^1\right) = i^{2L} = (-1)^{L_y}. \tag{26}$$

Mapped to bosonic side, it becomes a constraint:

$$W_y(\boldsymbol{r}) \equiv \Phi_{\boldsymbol{r}}^{12}\Phi_{\boldsymbol{r}+\boldsymbol{y}}^{12}\cdots\Phi_{\boldsymbol{r}-\boldsymbol{y}}^{12} = -1. \tag{27}$$

Notice that this constraint is independent of the choice of base point $\boldsymbol{r}$. Topologically the y loop is a homology class, whose various deformations can be achieved by plaquette constraints [Eq. (24)] in the last section. Along the x direction there is also a similar constraint

$$W_x(\boldsymbol{r}) \equiv \Phi_{\boldsymbol{r}}^{34}\Phi_{\boldsymbol{r}+\boldsymbol{x}}^{34}\cdots\Phi_{\boldsymbol{r}-\boldsymbol{x}}^{34} = -1. \tag{28}$$

From two classes of Wilson loop constraints we obtain a global constraint of fermion parity:

$$\begin{aligned}\hat{P} &\equiv \rho^{L_xL_y}\prod_{n=0}^{L_x-1}W_y(\boldsymbol{r}+n\boldsymbol{x})\prod_{n=0}^{L_y-1}W_x(\boldsymbol{r}+n\boldsymbol{y})\\ &= \rho^{L_xL_y}\prod_{m=0}^{L_x-1}\prod_{n=0}^{L_y-1}\Phi_{m\boldsymbol{x}+n\boldsymbol{y}}^{12}\Phi_{m\boldsymbol{x}+n\boldsymbol{y}}^{34}\\ &= \prod_{m=0}^{L_x-1}\prod_{n=0}^{L_y-1}\Theta_{m\boldsymbol{x}+n\boldsymbol{y}}^{12}\Theta_{m\boldsymbol{x}+n\boldsymbol{y}}^{34}\\ &\overset{c}{=} (-1)^{L_x+L_y}\rho^{L_xL_y},\end{aligned} \tag{29}$$

where we have used the parton parity on each site, $\Gamma_{\boldsymbol{r}} = \Theta_{\boldsymbol{r}}^{12}\Theta_{\boldsymbol{r}}^{34}\Phi_{\boldsymbol{r}}^{12}\Phi_{\boldsymbol{r}}^{34} = \rho$. On the fermionic side, $\Theta_{\boldsymbol{r}}^{12}\Theta_{\boldsymbol{r}}^{34}$ is equal to on-site fermion parity $(-1)^{n_{\boldsymbol{r}}}$, so the product over the lattice gives global fermion parity. Combining Wilson loop constraints and on-site parton parity fixing, we can describe half of the physical Hilbert space where fermion parities of states are fixed. For instance, to make the vacuum state parity even, L_x and L_y should be both odd or both even. In the former case ρ has to be $+1$ while in the latter case ρ can be either $+1$ or -1.

To describe the whole Hilbert space, we can consider bosonization of fermion-odd operators, like $\gamma_{\boldsymbol{r}}^\alpha$. The basic idea is that we may modify the fermion-boson mapping such that one of the L_xL_y Wilson loop constraints is violated so there is an extra minus sign in the expression of $\hat{P}$. This can be implemented by introducing a "defect" on a certain site, making an arrow of one link reversed. Then by checking the commutation relations we can regard a certain $\Lambda_{\boldsymbol{r}}^{\alpha x}$ as bosonization of $\gamma_{\boldsymbol{r}}^\alpha$ after such manipulations. This is similar to the case where we choose a starting point in one-dimensional (1D) Jordan-Wigner transformation so that fermion-odd operators are mapped to Pauli strings. For a square lattice this has been discussed in detail in Ref. [31]. We do not show details temporarily, but will discuss this in Sec. V B for cubic lattices.

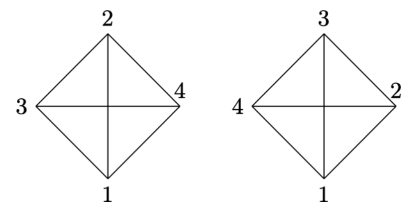

FIG. 2. Two choices of labeling. The right choice can be obtained by doing local unitary transformation of the left one.

C. Local permutations and symmetries

In the setup above, we have labeled the four auxiliary Majorana $\chi^{x'}$s in an antipodal way. One may ask if there is any preference in choosing a certain labeling order: in other words, what is the connection and difference between two artificial choices (see Fig. 2 for example)? It turns out that different choices of labeling are physically equivalent by local unitary transformations. To see this, we look for a SO(4) rotational transformation of χ^x from one labeling order to another as discussed in Sec. II. For instance, the transformation in Fig. 2 is

$$(\Lambda^{\alpha 1}\Lambda^{\alpha 2}\Lambda^{\alpha 3}\Lambda^{\alpha 4}) \Rightarrow (\Lambda^{\alpha 1}\ \Lambda^{\alpha 2}\ \Lambda^{\alpha 3}\ \Lambda^{\alpha 4})\begin{pmatrix}1&0&0&0\\0&0&0&1\\0&1&0&0\\0&0&1&0\end{pmatrix}. \tag{30}$$

The transformation matrix is a permutation operation with determinant 1 (if the determinant is -1 then one needs to add a minus sign before one nonvanishing entry to preserve orientation), and thus is an element in group SO(4). Generically we can find an antisymmetric real matrix A such that the transformation matrix is equal to e^{-2A}; then a unitary matrix $V(A) = e^{-i\sum_{xy}\phi^{xy}A_{xy}}$ will permute the second index of $\Lambda^{\alpha x}$. In the example above, the solution is

$$A = \frac{-1}{2}\begin{pmatrix}0&0&0&0\\0&0&-\frac{2\pi}{3\sqrt{3}}&\frac{2\pi}{3\sqrt{3}}\\0&\frac{2\pi}{3\sqrt{3}}&0&-\frac{2\pi}{3\sqrt{3}}\\0&-\frac{2\pi}{3\sqrt{3}}&\frac{2\pi}{3\sqrt{3}}&0\end{pmatrix}, \tag{31a}$$

$$V(A) = e^{-i\frac{2\pi}{3\sqrt{3}}(-\phi^{23}+\phi^{24}-\phi^{34})}. \tag{31b}$$

The example above does not touch physical symmetries. If we consider internal unitary symmetries, like charge conjugation and particle-hole symmetry, we can use $U(A)$ and $V(A)$ with different A matrices. For spatial symmetry trans-

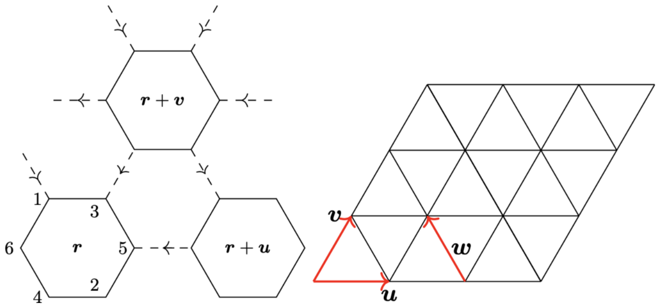

FIG. 3. The right figure is a triangular lattice with two basis vectors in red. The left figure shows that six auxiliary Majorana fermions are attached to each site, with labels 1 to 6.

formation, besides rotating the lattice sites (we call it "bare rotation"), we should also rotate both labels of χ's and intersite arrows correspondingly. For example, the C_4 rotation transformation can be represented by a combination of bare rotation C_4^b and internal unitary V_{C_4}:

$$C_4 = V_{C_4} C_4^b, \tag{32a}$$

$$C_4^b \Lambda_r^{44}\Lambda_{r+x}^{33}(\hat{C}_4^b)^{-1} = \Lambda_r^{44}\Lambda_{\hat{C}_4 r+y}^{33},$$
$$V_{C_4} = e^{-i\frac{\pi}{4}\sum_r\left(\phi_r^{12}+\phi_r^{34}-\sqrt{2}\left(\phi_r^{13}+\phi_r^{24}+\phi_r^{14}-\phi_r^{23}\right)\right)}, \tag{32b}$$

such that

$$(\Lambda^{\alpha 1}\ \Lambda^{\alpha 2}\ \Lambda^{\alpha 3}\ \Lambda^{\alpha 4}) \Rightarrow (-\Lambda^{\alpha 4}\ \Lambda^{\alpha 3}\ \Lambda^{\alpha 1}\ \Lambda^{\alpha 2}), \tag{33}$$

where we have added a minus sign to preserve the directions of arrows. For the square lattice more details of these transformations can be found in Ref. [31]. In this sense, our bosonization strategy makes symmetries of the lattice system manifest.

To conclude this section, we compare the present $\eta\chi$ construction with the approach in Ref. [31]. In Ref. [31], the parton construction is designed to implement a sense of spin-charge separation, so partons therein have different physical meaning. This can be regarded as choosing a different basis for the Clifford algebra generated by η^α and χ^x. In Appendix A, we show that qubit representation here can be turned into qubit representation (Eq. (112) in Ref. [31]) by a local unitary transformation. We also show that after imposing the parity constraint on the partons, the on-site Hilbert space for both approaches furnishes a spinor representation of SO(8), and states with the same weight on the two sides correspond to the same fermionic state.

IV. TRIANGULAR LATTICE

Our second example is the bosonization of a triangular lattice system (see Fig. 3). Each vertex has coordination number six. We will consider a spinful fermion, although it can be generalized to an arbitrary number of flavors.

For a triangular lattice, on each site there are six links, so similar to the square lattice case we start from χ^x, $x = 1, 2, \dots, 6$ and η^α, $\alpha = 1, 2, 3, 4$. The on-site Hilbert space is now $2^5 = 32$-dimensional. Based on the square lattice case, we extend the complex fermion representation to χ^5, χ^6:

$$\chi^5 = h + h^\dagger, \quad \chi^6 = i(h - h^\dagger). \tag{34}$$

The basis states of the on-site Hilbert space are in the form

$$|n_a n_b n_d n_g n_h\rangle = (a^\dagger)^{n_a}(b^\dagger)^{n_b}(d^\dagger)^{n_d}(g^\dagger)^{n_g}(h^\dagger)^{n_h}|0\rangle. \tag{35}$$

On each site we also define a parton parity operator and make projection to its eigenspace with eigenvalue ρ,

$$\Gamma_r \equiv -i^5\eta_r^1\eta_r^2\eta_r^3\eta_r^4\chi_r^1\chi_r^2\chi_r^3\chi_r^4\chi_r^5\chi_r^6 \overset{c}{=} \rho,$$
$$\Leftrightarrow \Theta_r^{12}\Theta_r^{34}\Phi_r^{12}\Phi_r^{34}\Phi_r^{56} = \rho. \tag{36}$$

A. Qubit representation

As shown in Eq. (35), we can use five qubits to represent the states similar to Eq. (19). For $\alpha, \beta \in \{1, 2, 3, 4\}$ the expressions of $\Theta^{\alpha\beta}$ are the same as in Eq. (21a). For other operators, one should notice that anticommutation relations bring extra Pauli Z operators.

The parity operator is $\Gamma_r = Z^{(1)}Z^{(2)}Z^{(3)}Z^{(4)}Z^{(5)}$. We fix $\Gamma_r = \rho \in \{+1, -1\}$ so that the last qubit can be hidden as in Eq. (22). Operations acting on the last qubit can be replaced by

$$\begin{aligned} X^{(5)} &\Rightarrow \mathbb{1}, \\ Z^{(5)} &\Rightarrow \rho Z^{(1)}Z^{(2)}Z^{(3)}Z^{(4)}, \\ Y^{(5)} &\Rightarrow i\rho Z^{(1)}Z^{(2)}Z^{(3)}Z^{(4)}. \end{aligned} \tag{37}$$

Then the $\Lambda^{\alpha x}$ matrix is

$$\Lambda^{\alpha x} = \begin{pmatrix} Y^{(1)}Z^{(2)}X^{(3)} & -Y^{(1)}Z^{(2)}Y^{(3)} & Y^{(1)}Z^{(2)}Z^{(3)}X^{(4)} & -Y^{(1)}Z^{(2)}Z^{(3)}Y^{(4)} & Y^{(1)}Z^{(2)}Z^{(3)}Z^{(4)} & \rho X^{(1)} \\ X^{(1)}Z^{(2)}X^{(3)} & -X^{(1)}Z^{(2)}Y^{(3)} & X^{(1)}Z^{(2)}Z^{(3)}X^{(4)} & -X^{(1)}Z^{(2)}Y^{(3)}Y^{(4)} & X^{(1)}Z^{(2)}Z^{(3)}Z^{(4)} & -\rho Y^{(1)} \\ Y^{(2)}X^{(3)} & -Y^{(2)}Y^{(3)} & Y^{(2)}Z^{(3)}X^{(4)} & -Y^{(2)}Z^{(3)}Y^{(4)} & Y^{(2)}Z^{(3)}Z^{(4)} & \rho Z^{(1)}X^{(2)} \\ X^{(2)}X^{(3)} & -X^{(2)}Y^{(3)} & X^{(2)}Z^{(3)}X^{(4)} & -X^{(2)}Z^{(3)}Y^{(4)} & X^{(2)}Z^{(3)}Z^{(4)} & -\rho Z^{(1)}Y^{(2)} \end{pmatrix}_{ij}. \tag{38}$$

We also list extra Φ operators besides Eq. (21c) for later use:

$$\begin{aligned} &\Phi^{56} = -Z^{(5)}, \\ &\Phi^{15} = Y^{(3)}Z^{(4)}X^{(5)}, \Phi^{16} = Y^{(3)}Z^{(4)}Y^{(5)}, \\ &\Phi^{25} = -X^{(3)}Z^{(4)}X^{(5)}, \Phi^{26} = X^{(3)}Z^{(4)}Y^{(5)}, \\ &\Phi^{35} = -Y^{(4)}X^{(5)}, \Phi^{36} = Y^{(4)}Y^{(5)}, \\ &\Phi^{45} = -X^{(4)}X^{(5)}, \Phi^{46} = X^{(4)}Y^{(5)}. \end{aligned} \tag{39}$$

We turn to plaquette constraints. For a triangular lattice there are two types of inequivalent plaquettes, which we denote as I and II. For instance, a type I plaquette gives the

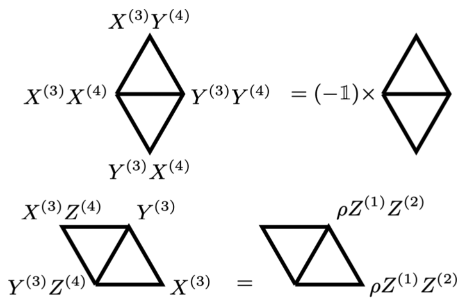

FIG. 4. The combined constraints.

constraint

$$\begin{aligned}-1 &= \left(i\gamma_{\boldsymbol r}^{i_1}\gamma_{\boldsymbol r}^{i_2}\right)\left(i\gamma_{\boldsymbol r}^{i_2}\gamma_{\boldsymbol r+\boldsymbol u}^{i_3}\right)\left(i\gamma_{\boldsymbol r+\boldsymbol u}^{i_3}\gamma_{\boldsymbol r+\boldsymbol u}^{i_4}\right)\left(i\gamma_{\boldsymbol r+\boldsymbol u}^{i_4}\gamma_{\boldsymbol r+\boldsymbol v}^{i_5}\right)\\ &\quad\times\left(i\gamma_{\boldsymbol r+\boldsymbol v}^{i_5}\gamma_{\boldsymbol r+\boldsymbol v}^{i_6}\right)\left(i\gamma_{\boldsymbol r+\boldsymbol v}^{i_6}\gamma_{\boldsymbol r}^{i_1}\right) \qquad (40)\\ &\to \hat C_{\boldsymbol r}^{\mathrm I} \equiv \Phi_{\boldsymbol r}^{35}\Phi_{\boldsymbol r+\boldsymbol u}^{61}\Phi_{\boldsymbol r+\boldsymbol v}^{24} \overset{c}{=} 1,\end{aligned}$$

where we choose $i_1 \neq i_2$, $i_3 \neq i_4$, $i_5 \neq i_6$, and the superscript "I" for $\hat C_{\boldsymbol r}^{\mathrm I}$ stands for type I plaquette. Similarly one can obtain the constraint for a type II plaquette:

$$\hat C_{\boldsymbol r}^{\mathrm{II}} \equiv \Phi_{\boldsymbol r}^{52}\Phi_{\boldsymbol r+\boldsymbol u-\boldsymbol v}^{13}\Phi_{\boldsymbol r+\boldsymbol u}^{46} \overset{c}{=} -1. \qquad (41)$$

Using the qubit representation of Φ^{xy} and replacements in Eq. (37), we obtain constraints in terms of Pauli matrices:

$$\begin{aligned}&\text{type I: } Y_{\boldsymbol r}^{(4)}X_{\boldsymbol r+\boldsymbol a}^{(3)}X_{\boldsymbol r+\boldsymbol v}^{(3)}Y_{\boldsymbol r+\boldsymbol v}^{(4)}\\ &= -\rho\left(Z^{(1)}Z^{(2)}\right)_{\boldsymbol r+\boldsymbol u},\\ &\times \text{ type II: } X_{\boldsymbol r}^{(3)}Z_{\boldsymbol r}^{(4)}Z_{\boldsymbol r+\boldsymbol u}^{(3)}Y_{\boldsymbol r+\boldsymbol u}^{(4)}Y_{\boldsymbol r+\boldsymbol u-\boldsymbol v}^{(3)}X_{\boldsymbol r+\boldsymbol u-\boldsymbol v}^{(4)} \qquad (42)\\ &= \rho\left(Z^{(1)}Z^{(2)}\right)_{\boldsymbol r+\boldsymbol u}.\end{aligned}$$

We can also combine these two constraints, up-down and left-right, as noted in Fig. 4. The second equation in the figure shows again similarity to Wen's plaquette model [43], if we consider all states in eigenstates of Pauli Z.

The counting of degrees of freedom is as follows. Each plaquette constraint is shared by three sites, so it contributes $\frac{1}{3}$ constraints for each site. Then each site effectively has $6 \times \frac{1}{3} = 2$ plaquette constraints. Combining the local parton parity projection, we get back to a physical Hilbert space.

B. Wilson loops

For triangular lattices with periodic boundary conditions, we can also understand the systems as if they are on a torus manifold. Suppose the system size is $L_a \times L_b$; we have two extra Wilson loop constraints as follows. In the $\boldsymbol u$ direction, we have

$$W_a(\boldsymbol r) \equiv \Phi_{\boldsymbol r}^{65}\Phi_{\boldsymbol r+\boldsymbol u}^{65}\cdots\Phi_{\boldsymbol r-\boldsymbol u}^{65} \overset{c}{=} -1. \qquad (43)$$

Similarly along the $\boldsymbol v$ direction,

$$W_b(\boldsymbol r) \equiv \Phi_{\boldsymbol r}^{43}\Phi_{\boldsymbol r+\boldsymbol v}^{43}\cdots\Phi_{\boldsymbol r-\boldsymbol v}^{43} \overset{c}{=} -1. \qquad (44)$$

There is a remaining type of loop along the $(\boldsymbol u - \boldsymbol v)$ direction, which can be expressed as products of Wilson loops along $\boldsymbol u$ and $\boldsymbol v$ directions and some plaquettes.

One may wonder if the system is overconstrained. Similar to the square lattice case, with periodic boundary conditions the product of all plaquette constraints is equal to the identity, meaning one of them is dependent on others. So finally we are left with a half Hilbert space with fixed global fermion parity, just like the discussions following Eq. (29).

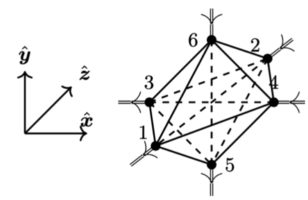

FIG. 5. Majorana fermions attached to a site in the cubic lattice with labels. The double lines with arrows represent the sign of mapping $i\gamma_{\boldsymbol r}^i\gamma_{\boldsymbol r'}^j$ to products of Λ's.

C. Symmetries

Besides translation symmetry along the $\boldsymbol u$ and $\boldsymbol v$ directions, the triangular lattice also has dihedral group symmetry D_6 generated by a 60° rotation C_6, and two reflections. C_6 rotational symmetry can be represented by bare rotation C_6^b and local unitary transformation. Bare C_6 rotation,

$$C_6^b : \Lambda_{\boldsymbol r}^{\alpha x} \Rightarrow \Lambda_{C_6\boldsymbol r}^{\alpha x}, \qquad (45)$$

and internal unitary transformation permutes χ indices

$$\begin{aligned}&(\Lambda^{\alpha 1}\ \Lambda^{\alpha 2}\ \Lambda^{\alpha 3}\ \Lambda^{\alpha 4}\ \Lambda^{\alpha 5}\ \Lambda^{\alpha 6})\\ &\quad\Rightarrow (\Lambda^{\alpha 6}\ -\Lambda^{\alpha 5}\ \Lambda^{\alpha 1}\ \Lambda^{\alpha 2}\ \Lambda^{\alpha 3}\ \Lambda^{\alpha 4}). \qquad (46)\end{aligned}$$

This can be realized by $V_{C_6} = e^{-i\pi/6\sum_{r,x,y}\phi_r^{xy}\tilde A_{xy}}$, where

$$\tilde A = \frac{1}{2}\begin{pmatrix} 0 & 1 & -2 & -\frac{2}{\sqrt3} & \frac{2}{\sqrt3} & 2\\ -1 & 0 & \frac{2}{\sqrt3} & -2 & -2 & \frac{2}{\sqrt3}\\ 2 & -\frac{2}{\sqrt3} & 0 & 1 & -2 & -\frac{2}{\sqrt3}\\ \frac{2}{\sqrt3} & 2 & -1 & 0 & \frac{2}{\sqrt3} & -2\\ -\frac{2}{\sqrt3} & 2 & 2 & -\frac{2}{\sqrt3} & 0 & 1\\ -2 & -\frac{2}{\sqrt3} & \frac{2}{\sqrt3} & 2 & -1 & 0 \end{pmatrix}. \qquad (47)$$

Reflection with respect to the $\boldsymbol u$ axis leads to

$$\begin{aligned}&(\Lambda^{\alpha 1}\ \Lambda^{\alpha 2}\ \Lambda^{\alpha 3}\ \Lambda^{\alpha 4}\ \Lambda^{\alpha 5}\ \Lambda^{\alpha 6})\\ &\quad\Rightarrow (-\Lambda^{\alpha 4}\ \Lambda^{\alpha 3}\ -\Lambda^{\alpha 2}\ \Lambda^{\alpha 1}\ \Lambda^{\alpha 3}\ \Lambda^{\alpha 4}), \qquad (48)\end{aligned}$$

so the reflection operator is a bare reflection $M_{\boldsymbol u}^b$ with a unitary operator $V_{M_{\boldsymbol u}}$,

$$M_{\boldsymbol u} = V_{M_{\boldsymbol u}}M_{\boldsymbol u}^b, \quad V_{M_{\boldsymbol u}} = e^{-\frac{\pi}{2}\sum_r(\phi_r^{23}-\phi_r^{14})}. \qquad (49)$$

Similarly, reflection with respect to the $(\hat{\boldsymbol u} + \hat{\boldsymbol v})$ axis is

$$\begin{aligned}M_{\hat{\boldsymbol u}+\hat{\boldsymbol v}} &= V_{M_{\hat{\boldsymbol u}+\hat{\boldsymbol v}}}M_{\hat{\boldsymbol u}+\hat{\boldsymbol v}}^b,\\ V_{M_{\hat{\boldsymbol u}+\hat{\boldsymbol v}}} &= e^{-\frac{\pi}{2}\sum_r\left(\phi_r^{12}+\phi_r^{34}+\phi_r^{45}+\phi_r^{56}-\phi_r^{36}\right)}.\end{aligned} \qquad (50)$$

V. CUBIC LATTICE

In this section, we discuss how to apply our $\eta\chi$ formalism to the 3D cubic lattice (see Fig. 5). Compared to the 2D lattice system, the plaquette constraints in 3D lattice systems become more complicated since visually there are many more

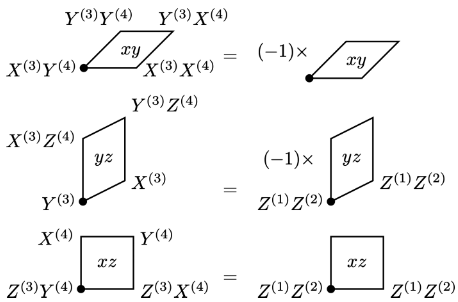

FIG. 6. Constraints for three types of plaquettes.

cycles and many of them are not independent. Since the cubic lattice is also six coordinated, the operator content is the same as in the triangular lattice. We first consider plaquette constraints and global constraints, with details on how to bosonize fermion-odd operators through the introduction of a "decorated link" [31]. We then discuss various symmetries in the cubic lattice. We show strategies for finding independent plaquette constraints in Appendix B.

A. Qubit representation

All operators $\Theta_{\boldsymbol{r}}^{\alpha\beta}$, $\Lambda_{\boldsymbol{r}}^{\alpha x}$, and $\Phi_{\boldsymbol{r}}^{xy}$ are the same as in the triangular case. Differences appear in the plaquette constraints. In a cubic lattice there are three types of plaquettes; we can call them the xy plaquette, yz plaquette, and xz plaquette:

$$\begin{aligned} xy: &\quad \hat{C}_{xy,\boldsymbol{r}} \equiv \Phi_{\boldsymbol{r}}^{24}\Phi_{\boldsymbol{r}+\boldsymbol{x}}^{32}\Phi_{\boldsymbol{r}+\boldsymbol{x}+\boldsymbol{y}}^{13}\Phi_{\boldsymbol{r}+\boldsymbol{y}}^{41} \overset{c}{=} -1,\\ yz: &\quad \hat{C}_{yz,\boldsymbol{r}} \equiv \Phi_{\boldsymbol{r}}^{62}\Phi_{\boldsymbol{r}+\boldsymbol{y}}^{16}\Phi_{\boldsymbol{r}+\boldsymbol{y}+\boldsymbol{z}}^{51}\Phi_{\boldsymbol{r}+\boldsymbol{z}}^{25} \overset{c}{=} -1,\\ xz: &\quad \hat{C}_{xz,\boldsymbol{r}} = \Phi_{\boldsymbol{r}}^{64}\Phi_{\boldsymbol{r}+\boldsymbol{x}}^{36}\Phi_{\boldsymbol{r}+\boldsymbol{x}+\boldsymbol{z}}^{53}\Phi_{\boldsymbol{r}+\boldsymbol{z}}^{45} \overset{c}{=} -1. \end{aligned} \tag{51}$$

These three constraints are not fully independent. To see this, we first assume the cubic lattice has open boundary conditions at least for one direction, for example, the $\boldsymbol{y}$ direction. Then consider a cube. Applying constraint equations to the pair of xy surfaces and the pair of yz surfaces, and by multiplying these equations, we get a product of the pair of xz constraints. We can pick up cubes contiguously along the $\boldsymbol{y}$ direction, so xz interfaces of these cubes cancel with each other, leaving finally

$$\hat{C}_{xz,\boldsymbol{r}}\hat{C}_{xz,\boldsymbol{L}_y} = 1, \tag{52}$$

where $\boldsymbol{r} = (r_x, r_y, r_z)$, $\boldsymbol{L}_y = (r_x, L_y, r_z)$, i.e., $\boldsymbol{L}_y$ is the projection of $\boldsymbol{y}$ to the boundary of the $\boldsymbol{y}$ direction. As long as we fix the boundary xz constraints, in the bulk all xz constraints are automatically true from the other two types of constraints. If the system is periodic in all three directions, i.e., on a 3-torus manifold, then we may choose a reference xz plane, and it is enough to fix the constraints on this xz plane rather than imposing three constraints for each cube. Graphically we show these constraints in Fig. 6.

We remark that although these three types of constraints are not independent, it is advantageous to keep track of all of them to simplify computing in real applications. We also notice that although we have used parton parity projection, the final forms of plaquette constraints are independent of which subspace of $\Gamma_{\boldsymbol{r}}$ the states are projected to.

B. Wilson loops and fermion-odd operators

If the system is on a three-dimensional torus, i.e., having three periodic boundary conditions, then we have three Wilson loop constraints. For instance, the fermion loop along the x direction gives the identity

$$\left(i\gamma_{\boldsymbol{r}}^3\gamma_{\boldsymbol{r}}^4\right)\left(i\gamma_{\boldsymbol{r}}^4\gamma_{\boldsymbol{r}+\boldsymbol{x}}^3\right)\cdots\left(i\gamma_{\boldsymbol{r}-\boldsymbol{x}}^4\gamma_{\boldsymbol{r}}^3\right) = (-1)^{L_x}. \tag{53}$$

Similarly we have constraints for y and z directions. Mapping these to bosonic operators, we obtain

$$\begin{aligned} W_x(\boldsymbol{r}) &\equiv \prod_{n=0}^{L_x-1}\Phi_{\boldsymbol{r}+n\boldsymbol{x}}^{12} \overset{c}{=} -1,\\ W_y(\boldsymbol{r}) &\equiv \prod_{n=0}^{L_y-1}\Phi_{\boldsymbol{r}+n\boldsymbol{y}}^{34} \overset{c}{=} -1,\\ W_z(\boldsymbol{r}) &\equiv \prod_{n=0}^{L_z-1}\Phi_{\boldsymbol{r}+n\boldsymbol{z}}^{56} \overset{c}{=} -1. \end{aligned} \tag{54}$$

As we mentioned, the three types of plaquette constraints are not independent, so we have to be careful to choose independent constraints for the whole system. The general counting is discussed in Sec. II C, and we give a set of generators explicitly in Appendix B.

For the cubic lattice, we define

$$\begin{aligned} \hat{P} &\equiv \rho^{L_xL_yL_z}\prod_{\boldsymbol{r},r_x=0}W_x(\boldsymbol{r})\prod_{\boldsymbol{r},r_y=0}W_y(\boldsymbol{r})\prod_{\boldsymbol{r},r_z=0}W_z(\boldsymbol{r})\\ &= \rho^{L_xL_yL_z}\prod_{\boldsymbol{r}}\Phi_{\boldsymbol{r}}^{12}\Phi_{\boldsymbol{r}}^{34}\Phi_{\boldsymbol{r}}^{56}\\ &= \prod_{\boldsymbol{r}}\Theta_{\boldsymbol{r}}^{12}\Theta_{\boldsymbol{r}}^{34}\Theta_{\boldsymbol{r}}^{56}\\ &\overset{c}{=} (-1)^{L_x+L_y+L_z}\rho^{L_xL_yL_z}. \end{aligned} \tag{55}$$

The last line shows that if L_x, L_y, and L_z are all odd, the parity is $-\rho$; if one of them is odd, the parity is -1; otherwise, the parity is $+1$. For the odd-parity case we cannot describe a fermion-even vacuum state, unless we release some of the constraints above. In general, if we want to describe the whole Hilbert space with different fermion parities, we should expect that some fermion-odd operators are also mapped to bosonic side.

In Ref. [31], this is done by introducing a "decorated link" to the square lattice. The basic idea is that in our mapping between the fermionic side and bosonic side, there is some artificial choice of corresponding signs; i.e., the algebra will be the same for $\pm i\gamma_{\boldsymbol{r}}^i\gamma_{\boldsymbol{r}'}^j \to \Lambda_{\boldsymbol{r}}^{ii}\Lambda_{\boldsymbol{r}'}^{jj}$ for neighboring sites $\boldsymbol{r}, \boldsymbol{r}'$. By reversing the direction of one of the mapping arrows, four plaquette constraints (living on faces attaching to the edge $\boldsymbol{rr}'$) and one Wilson loop constraint will have their signs reversed. In practice, we consider

$$i\gamma_{-\boldsymbol{x}}^4\gamma_{\boldsymbol{0}}^3 \to -\Lambda_{-\boldsymbol{x}}^{44}\Lambda_{\boldsymbol{0}}^{33}. \tag{56}$$

Under this mapping, the modified Wilson loop constraint is now $W_x(n\boldsymbol{x}) = +1$, $0 \leqslant n \leqslant L_x - 1$, and signs of four plaquette constraints are also reversed.

Consider $\Lambda_{\boldsymbol{0}}^{33}$, it is anticommuting with $\Theta_{\boldsymbol{0}}^{\alpha 3}$, $\alpha \neq 3$, and commuting with other $\Theta_{\boldsymbol{0}}^{\alpha\beta}$s. $\Lambda_{\boldsymbol{0}}^{33}$ also commutes with the decorated link $-\Lambda^{44}_{-x}\Lambda^{33}_{0}$. We remind that $\Theta^{\alpha 3}_{0} \leftrightarrow i\gamma^{\alpha}_{0}\gamma^{3}_{0}$. It is clear that Λ^{33}_{0} has the same commutation relations with fermion-odd operator γ^{3}_{0}. Based on this identification, we can map arbitrary Majorana operators in the lattice to the bosonic side and thus all fermion-odd operators, by a few number of $\Phi^{xy'}$s connecting intermediate sites. For instance, γ^2_{x} can be expressed as follows:

$$\begin{aligned}\gamma^2_{x} &= i\gamma^3_{0}\cdot\left(i\gamma^3_{0}\gamma^4_{0}\right)\left(i\gamma^4_{0}\gamma^3_{x}\right)\left(i\gamma^3_{x}\gamma^2_{x}\right)\\ &\to i\Lambda^{33}_{0}\Theta^{34}_{0}\Lambda^{44}_{0}\Lambda^{33}_{x}\Theta^{32}_{x} = -i\Phi^{34}_{0}\Lambda^{23}_{x}.\end{aligned} \tag{57}$$

In defining the map of fermion-odd operators we have chosen a link to modify the mapping, and one may ask whether the choice is special, since the lattice is homogeneous and a decorated link appears superficially like a defect. Actually, different positions of the decorated link can be related by a unitary operator $\hat{\mathcal{M}}(\Phi)$,

$$\hat{\mathcal{M}}(\Phi) = \frac{1+\hat{P}}{2} + \frac{1-\hat{P}}{2}\Phi, \tag{58}$$

where Φ represents a Jordan-Wigner string of Φ^{xy}_{r}. $\hat{P}$ commutes with an arbitrary Jordan-Wigner string Φ. Meanwhile, an operator in the form of products of Φ^{xy}_{r} and $\Lambda^{\alpha' x'}_{r}$ will commute or anticommute with $\hat{P}$ and Jordan-Wigner string Φ.

We briefly show $\hat{M}$ moves the decorated link in the following example and refer to Ref. [31] for details. Considering γ^2_{x} again, we can take $\Phi = -\Phi^{34}_{0}\Phi^{32}_{x}$, then one can readily find

$$\hat{\mathcal{M}}(\Phi)\left(i\Phi^{34}_{0}\Lambda^{23}_{x}\right)\hat{\mathcal{M}}(\Phi)^{\dagger} = \Lambda^{22}_{x}. \tag{59}$$

This means that, after unitary transformation of $\hat{\mathcal{M}}(\Phi)$, γ^2_{x} is mapped to Λ^{22}_{x}. Furthermore, one can find

$$\begin{aligned}\hat{\mathcal{M}}(\Phi)\left(-\Lambda^{44}_{-x}\Lambda^{33}_{0}\right)\hat{\mathcal{M}}(\Phi)^{\dagger} &= \Lambda^{44}_{-x}\Lambda^{33}_{0},\\ \hat{\mathcal{M}}(\Phi)\left(\Lambda^{22}_{x}\Lambda^{11}_{x+y}\right)\hat{\mathcal{M}}(\Phi)^{\dagger} &= -\Lambda^{22}_{x}\Lambda^{11}_{x+y},\end{aligned} \tag{60}$$

which means the decorated link is moved to $i\gamma^2_{x}\gamma^1_{x+y} \to -\Lambda^{22}_{x}\Lambda^{11}_{x+y}$.

C. Symmetries

In this section we discuss how spatial symmetries of the cubic lattice are represented on the bosonic side.

First we consider translation symmetry $T_{R} : \mathcal{O}_{r} \mapsto \mathcal{O}_{r+R}$. For the odd fermion parity case we have to move the decorated link simultaneously. Similar to discussions in the previous section, we can use $\hat{\mathcal{M}}(\Phi)$ to move the decorated link along three axes:

$$T_x = \hat{\mathcal{M}}\left(\Phi^{34}_{0}\right)T^b_x, \tag{61a}$$

$$T_y = \hat{\mathcal{M}}\left(\Phi^{32}_{0}\Phi^{13}_{y}\right)T^b_y, \tag{61b}$$

$$T_z = \hat{\mathcal{M}}\left(\Phi^{36}_{0}\Phi^{53}_{z}\right)T^b_z. \tag{61c}$$

Next, consider reflection with respect to the yz plane. The bare reflection M^b_x flips the sign of x coordinates for all sites. Meanwhile the auxiliary Majoranas should be reflected as follows:

$$\begin{aligned}&(\Lambda^{\alpha 1}\ \Lambda^{\alpha 2}\ \Lambda^{\alpha 3}\ \Lambda^{\alpha 4}\ \Lambda^{\alpha 5}\ \Lambda^{\alpha 6})\\ &\quad\Rightarrow (\Lambda^{\alpha 1}\ \Lambda^{\alpha 2}\ -\Lambda^{\alpha 4}\ \Lambda^{\alpha 3}\ \Lambda^{\alpha 5}\ \Lambda^{\alpha 6}).\end{aligned} \tag{62}$$

For odd fermion parity case, the decorated link is not moved during reflection. So combining internal unitary transformation and bare reflection, the full reflection can be achieved with

$$M_x = V_{M_x}M^b_x, \quad V_{M_x} = e^{-i\frac{\pi}{2}\sum_r \phi^{34}_r}. \tag{63}$$

Similarly reflections with respect to the zx plane and xy plane can be achieved with

$$M_y = V_{M_y}M^b_y, \quad V_{M_y} = e^{-i\frac{\pi}{2}\sum_r \phi^{12}_r}, \tag{64a}$$

$$M_z = V_{M_z}M^b_z, \quad V_{M_z} = e^{-i\frac{\pi}{2}\sum_r \phi^{56}_r}. \tag{64b}$$

For rotations of cubic lattice, there are three fourfold axes, four threefold axes, and six twofold axes. The rotation around the z axis is similar to the discussion in the square lattice case [Eq. (32)], where we just need to composite C_4 with an extra $\hat{\mathcal{M}}(\Phi^{31})$ so as to move the decorated link. So here we focus on other axes. Details of transformation matrices of all these axes are collected in Appendix C. Here we first consider 180° rotation around the 2-axis [110]. It is a bare rotation $C^b_{2,[110]}$ accompanied by a internal unitary which transforms

$$\begin{aligned}&(\Lambda^{\alpha 1}\ \Lambda^{\alpha 2}\ \Lambda^{\alpha 3}\ \Lambda^{\alpha 4}\Lambda^{\alpha 5}\ \Lambda^{\alpha 6})\\ &\quad\Rightarrow (\Lambda^{\alpha 3}\ \Lambda^{\alpha 4}\ \Lambda^{\alpha 1}\ \Lambda^{\alpha 2}\ -\Lambda^{\alpha 6}\ \Lambda^{\alpha 5}).\end{aligned} \tag{65}$$

The full rotation is

$$\begin{aligned}C_{2,[110]} &= \hat{\mathcal{M}}(\Phi^{31}_{r})V_{C_{2,[110]}}C^b_{2,[110]},\\ V_{C_{2,[110]}} &= e^{-i\frac{\pi}{2}\sum_r\left(\phi^{12}_r+\phi^{23}_r+\phi^{34}_r-\phi^{14}_r-\phi^{56}_r\right)}.\end{aligned} \tag{66}$$

For 120° rotation around the 3-axis [111], the internal unitary transforms as

$$(\Lambda^{\alpha 1}\ \Lambda^{\alpha 2}\ \Lambda^{\alpha 3}\ \Lambda^{\alpha 4}\ \Lambda^{\alpha 5}\ \Lambda^{\alpha 6}) \Rightarrow (\Lambda^{\alpha 5}\ \Lambda^{\alpha 6}\ \Lambda^{\alpha 1}\ \Lambda^{\alpha 2}\ \Lambda^{\alpha 3}\ \Lambda^{\alpha 4}). \tag{67}$$

The full rotation is

$$\begin{aligned}C_{3,[111]} &= \hat{\mathcal{M}}(\Phi^{31}_{r})V_{C_{3,[111]}}C^b_{3,[111]},\\ V_{C_{3,[111]}} &= e^{-i\frac{2\pi}{3}\sum_r\frac{1}{\sqrt{3}}\left(\phi^{15}_r+\phi^{26}_r-\phi^{13}_r-\phi^{24}_r-\phi^{35}_r-\phi^{46}_r\right)}.\end{aligned} \tag{68}$$

VI. EXAMPLE: CHIRAL *p*-WAVE SUPERCONDUCTOR ON TRIANGULAR LATTICE

As a concrete example, we apply our bosonization to a chiral p-wave superconductor model on a triangular lattice (Fig. 3).

An example of a Bogoliubov–de Gennes (BdG) Hamiltonian of a chiral p-wave superconductor for a triangular lattice is

$$\begin{aligned}\hat{H} &= \frac{1}{2}\sum_{k}(c^{\dagger}_{k}\ c_{-k})\begin{pmatrix}\varepsilon_k & \Delta(k)\\ \Delta(k)^{\dagger} & -\varepsilon_k\end{pmatrix}\begin{pmatrix}c_k\\ c^{\dagger}_{-k}\end{pmatrix},\\ \varepsilon_k &= 4t-\mu-\frac{4t}{3}(\cos k\cdot u+\cos k\cdot v+\cos k\cdot w),\\ \Delta(k) &= -i\Delta_0(\sin k\cdot u+\phi\sin k\cdot v+\phi^2\sin k\cdot w),\end{aligned} \tag{69}$$

where Δ_0 is a real number representing the energy gap, and $\phi = e^{i\pi/3}$ is a phase factor. Here $\boldsymbol{u}$, $\boldsymbol{v}$, and $\boldsymbol{w}$ are lattice vectors defined in Fig. 3. Expanding near the $\boldsymbol{k} = 0$ point, and setting $t = \frac{1}{2m}$, we see that the BdG Hamiltonian reduces to

$$H(\boldsymbol{k}) = \begin{pmatrix} \frac{k^2}{2m} - \mu & -i\frac{3}{2}\Delta_0(k_x + ik_y) \\ i\frac{3}{2}\Delta_0(k_x - ik_y) & -\left(\frac{k^2}{2m} - \mu\right) \end{pmatrix}. \tag{70}$$

For a fixed hopping coefficient t, the chemical potential μ can be tuned to present different topological phases. By Fourier transformation we obtain the real space Hamiltonian,

$$\begin{aligned} H = \sum_{\boldsymbol{r}} & -t(c_{\boldsymbol{r}}^\dagger c_{\boldsymbol{r}+\boldsymbol{u}} + c_{\boldsymbol{r}}^\dagger c_{\boldsymbol{r}+\boldsymbol{v}} + c_{\boldsymbol{r}}^\dagger c_{\boldsymbol{r}+\boldsymbol{w}} + h.c.) \\ & + (4t - \mu) c_{\boldsymbol{r}}^\dagger c_{\boldsymbol{r}} \\ & + \Delta_0 (c_{\boldsymbol{r}}^\dagger c_{\boldsymbol{r}+\boldsymbol{u}}^\dagger + \phi c_{\boldsymbol{r}}^\dagger c_{\boldsymbol{r}+\boldsymbol{v}}^\dagger + \phi^2 c_{\boldsymbol{r}}^\dagger c_{\boldsymbol{r}+\boldsymbol{w}}^\dagger + \text{H.c.}). \end{aligned} \tag{71}$$

For simplicity we rescale $\frac{2t}{3} \to t$ from now. To bosonize, we first turn the complex fermions into Majorana fermions: $c_{\boldsymbol{r}} = \frac{1}{2}(\gamma_{\boldsymbol{r}} - i\gamma_{\boldsymbol{r}}^2)$, $c_{\boldsymbol{r}}^\dagger = \frac{1}{2}(\gamma_{\boldsymbol{r}} + i\gamma_{\boldsymbol{r}}^2)$. In Majorana representation,

$$H = H_{\boldsymbol{u}} + H_{\boldsymbol{v}} + H_{\boldsymbol{w}} + H_0,$$

$$\begin{aligned} H_0 &= -(4t - \mu) \sum_{\boldsymbol{r}} i\gamma_{\boldsymbol{r}}^1 \gamma_{\boldsymbol{r}}^2, \\ H_{\boldsymbol{u}} &= \frac{1}{4} \sum_{\boldsymbol{r}} (-t + \Delta_0)\left(\gamma_{\boldsymbol{r}}^1 \gamma_{\boldsymbol{r}+\boldsymbol{u}}^1 + i\gamma_{\boldsymbol{r}}^2 \gamma_{\boldsymbol{r}+\boldsymbol{u}}^1\right) \\ &\quad + (-t - \Delta_0)\left(\gamma_{\boldsymbol{r}}^2 \gamma_{\boldsymbol{r}+\boldsymbol{u}}^2 - i\gamma_{\boldsymbol{r}}^1 \gamma_{\boldsymbol{r}+\boldsymbol{u}}^2\right) + \text{H.c.} \\ &= \frac{1}{2} \sum_{\boldsymbol{r}} (-t + \Delta_0) i\gamma_{\boldsymbol{r}}^2 \gamma_{\boldsymbol{r}+\boldsymbol{u}}^1 + (t + \Delta_0) i\gamma_{\boldsymbol{r}}^1 \gamma_{\boldsymbol{r}+\boldsymbol{u}}^2, \\ H_{\boldsymbol{v}} &= \frac{1}{4} \sum_{\boldsymbol{r}} (-t + \phi\Delta_0)\left(\gamma_{\boldsymbol{r}}^1 \gamma_{\boldsymbol{r}+\boldsymbol{v}}^1 + i\gamma_{\boldsymbol{r}}^2 \gamma_{\boldsymbol{r}+\boldsymbol{v}}^1\right) \\ &\quad + (-t - \phi\Delta_0)\left(\gamma_{\boldsymbol{r}}^2 \gamma_{\boldsymbol{r}+\boldsymbol{v}}^2 - i\gamma_{\boldsymbol{r}}^1 \gamma_{\boldsymbol{r}+\boldsymbol{v}}^2\right) + \text{H.c.} \\ &= \frac{1}{2} \sum_{\boldsymbol{r}} (-t + \phi\Delta_0) i\gamma_{\boldsymbol{r}}^2 \gamma_{\boldsymbol{r}+\boldsymbol{v}}^1 + (t + \phi\Delta_0) i\gamma_{\boldsymbol{r}}^1 \gamma_{\boldsymbol{r}+\boldsymbol{v}}^2, \\ H_{\boldsymbol{w}} &= \frac{1}{4} \sum_{\boldsymbol{r}} (-t + \phi^2\Delta_0)\left(\gamma_{\boldsymbol{r}}^1 \gamma_{\boldsymbol{r}+\boldsymbol{w}}^1 + i\gamma_{\boldsymbol{r}}^2 \gamma_{\boldsymbol{r}+\boldsymbol{w}}^1\right) \\ &\quad + (-t - \phi^2\Delta_0)\left(\gamma_{\boldsymbol{r}}^2 \gamma_{\boldsymbol{r}+\boldsymbol{w}}^2 - i\gamma_{\boldsymbol{r}}^1 \gamma_{\boldsymbol{r}+\boldsymbol{w}}^2\right) + \text{H.c.} \\ &= \frac{1}{2} \sum_{\boldsymbol{r}} (-t + \phi^2\Delta_0) i\gamma_{\boldsymbol{r}}^2 \gamma_{\boldsymbol{r}+\boldsymbol{w}}^1 + (t + \phi^2\Delta_0) i\gamma_{\boldsymbol{r}}^1 \gamma_{\boldsymbol{r}+\boldsymbol{w}}^2. \end{aligned} \tag{72}$$

After bosonization, it turns out to be

$$H_0 \longrightarrow H_0^B = -(4t - \mu) \sum_{\boldsymbol{r}} \Theta_{\boldsymbol{r}}^{12} = -(4t - \mu) \sum_{\boldsymbol{r}} Z_{\boldsymbol{r}}^{(1)}, \tag{73a}$$

$$\begin{aligned} H_{\boldsymbol{u}} \longrightarrow H_{\boldsymbol{u}}^B &= \frac{1}{2} \sum_{\boldsymbol{r}} (-t + \Delta_0) \Lambda_{\boldsymbol{r}}^{25} \Lambda_{\boldsymbol{r}+\boldsymbol{u}}^{16} + (t + \Delta_0) \Lambda_{\boldsymbol{r}}^{15} \Lambda_{\boldsymbol{r}+\boldsymbol{u}}^{26} \\ &= \frac{1}{2} \sum_{\boldsymbol{r}} (-t + \Delta_0) X_{\boldsymbol{r}}^{(1)} Z_{\boldsymbol{r}}^{(2)} Z_{\boldsymbol{r}}^{(3)} \left(-X_{\boldsymbol{r}+\boldsymbol{u}}^{(1)}\right) + (t + \Delta_0) Y_{\boldsymbol{r}}^{(1)} Z_{\boldsymbol{r}}^{(2)} Z_{\boldsymbol{r}}^{(3)} \left(Y_{\boldsymbol{r}+\boldsymbol{u}}^{(1)}\right), \end{aligned} \tag{73b}$$

$$\begin{aligned} H_{\boldsymbol{v}} \longrightarrow H_{\boldsymbol{v}}^B &= \frac{1}{2} \sum_{\boldsymbol{r}} (-t + \phi\Delta_0) \Lambda_{\boldsymbol{r}}^{23} \Lambda_{\boldsymbol{r}+\boldsymbol{v}}^{14} + (t + \phi\Delta_0) \Lambda_{\boldsymbol{r}}^{13} \Lambda_{\boldsymbol{r}+\boldsymbol{v}}^{24} \\ &= \frac{1}{2} \sum_{\boldsymbol{r}} (-t + \phi\Delta_0) X_{\boldsymbol{r}}^{(1)} Z_{\boldsymbol{r}}^{(2)} X_{\boldsymbol{r}}^{(3)} \left(-Y^{(1)} Z^{(2)} Y^{(3)}\right)_{\boldsymbol{r}+\boldsymbol{v}} + (t + \phi\Delta_0) Y_{\boldsymbol{r}}^{(1)} Z_{\boldsymbol{r}}^{(2)} X_{\boldsymbol{r}}^{(3)} \left(-X^{(1)} Z^{(2)} Y^{(3)}\right)_{\boldsymbol{r}+\boldsymbol{v}}, \end{aligned} \tag{73c}$$

$$\begin{aligned} H_{\boldsymbol{w}} \longrightarrow H_{\boldsymbol{w}}^B &= \frac{1}{2} \sum_{\boldsymbol{r}} (-t + \Delta_0) \Lambda_{\boldsymbol{r}}^{21} \Lambda_{\boldsymbol{r}+\boldsymbol{w}}^{12} + (t + \Delta_0) \Lambda_{\boldsymbol{r}}^{11} \Lambda_{\boldsymbol{r}+\boldsymbol{w}}^{22} \\ &= \frac{1}{2} \sum_{\boldsymbol{r}} (-t + \phi^2\Delta_0) X_{\boldsymbol{r}}^{(1)} X_{\boldsymbol{r}}^{(2)} \left(-Y^{(1)} Y^{(2)}\right)_{\boldsymbol{r}+\boldsymbol{w}} + (t + \phi^2\Delta_0) Y_{\boldsymbol{r}}^{(1)} X_{\boldsymbol{r}}^{(2)} \left(-X^{(1)} Y^{(2)}\right)_{\boldsymbol{r}+\boldsymbol{w}}. \end{aligned} \tag{73d}$$

In the above equations, we have used the Majorana parton parity constraints to eliminate one qubit per site. The qubit representation follows directly from Eq. (38) by freezing the spin degree of freedom of original fermions. Besides these terms, we also include the plaquette constraint terms into the bosonized Hamiltonian, $H^B = H_0^B + H_{\boldsymbol{u}}^B + H_{\boldsymbol{v}}^B + H_{\boldsymbol{w}}^B + H_{\text{plaquettes}}$. This model can then be interpreted as an exactly solved chiral spin liquid emerging from our bosonization of a triangular lattice p-wave superconductor.

The emergence of quantum spin liquid models is general in our bosonization scheme, due to the emergent plaquette constraints. If we start from an exactly solvable fermion problem, like free fermion problems, we should expect the obtained spin liquid to be also solvable. From this perspective, our bosonization scheme provides a way to engineer quantum spin liquid models, while preserving symmetries manifestly. It will be interesting to study the interplay between topological order and spontaneous symmetry breaking from a bosonization perspective.

VII. DISCUSSIONS

In this work, we discuss how symmetries could stay manifest on the bosonic side under a higher-dimensional

Jordan-Wigner transformation, similar in spirit to the approach in Ref. [31]. While the approach presented here can be traced to the existing discussions on the bosonization of lattice fermions through the introduction of a $\mathbb{Z}_2$ lattice gauge field and, associated with them, Majorana fermions [7,9,27], our main focus is on how the symmetries, especially spatial ones, are represented on the bosonic side for the physically interesting cases of the square, triangular, and cubic lattices. As described, however, our formalism applies only to even-coordinated lattices. In the following, we describe how sites with odd coordination number could be treated, and also draw connections to earlier works related to the design of exactly solved spin liquid models.

First, we address the issue of lattices with odd coordination numbers. As discussed in Sec. III B, by counting the constraints it can be seen that $\eta\chi$ construction is in principle suitable for all kinds of graphs, at least in terms of the Hilbert space dimension. But if some vertices in the graph have odd coordination numbers, then our approach requires introducing an odd number of χ's on the site, and so we do not have a valid on-site Hilbert space unless the number of η's is also odd.

Given the number of η Majorana fermions is fixed by the physical problem of interest, the $\eta\chi$ approach as we discussed is applicable to lattices with oddly coordinated sites only if we start with an odd number of Majorana fermions on such sites. In contrast, most models of interest in condensed matter physics are defined using complex fermions (at least those describing electrons hopping on a lattice), and so the number of Majorana fermions is always even on each site. One possible resolution to this dilemma is to recognize that the graph defining the operator content, and hence the effective coordination number of a site (more accurately, its degree as a vertex on the graph) is not as rigid as it may seem. One could add additional edges to the graph while maintaining the symmetries, such that all sites effectively become even coordinated. For instance, consider the trivalent honeycomb lattice. Each site has three nearest neighbors, six second-nearest neighbors, and three third-nearest neighbors. Therefore, by including also links between third-nearest neighbors each site becomes six coordinated, and we could proceed with the $\eta\chi$ construction without spoiling any spatial symmetries. A trade-off, however, is that we introduce more degrees of freedom on the bosonic side, and that there are more loops and hence constraints.

The present $\eta\chi$ formalism can also be related to some well-known quantum spin liquid models. For example, Kitaev's honeycomb model [38] has Majorana fermion representations, and our $\eta\chi$ formalism can also be used to obtain such models in a natural way. We present two examples here: one is Kitaev's honeycomb model, and the other is Ryu's diamond model [39]. One important feature here is that the fermionic system is taken to be emergent instead of physical, and as such there is no restriction on the number of η Majorana fermions per site. It will be natural to leverage such freedom and consider an odd (even) number of η fermions on sites with odd (even) coordination numbers.

Consider a honeycomb lattice with one Majorana fermion mode per site. In the $\eta\chi$ formalism $\Lambda^{\alpha x}$ is then a 1×3 matrix; i.e., there are one η and three χ's per site. Nearest-neighbor fermion bilinear $i\gamma_{\boldsymbol{r}}\gamma_{\boldsymbol{r}+\boldsymbol{e}_j}$ then gets mapped to $\Lambda_{\boldsymbol{r}}^{1j}\Lambda_{\boldsymbol{r}+\boldsymbol{e}_j}^{1j}$ for $j = 1, 2, 3$ denoting the three neighbor links. Since any two operators among $\{\Lambda_{\boldsymbol{r}}^{11}, \Lambda_{\boldsymbol{r}}^{12}, \Lambda_{\boldsymbol{r}}^{13}\}$ should anticommute, and the site Hilbert space is two dimensional (four auxiliary Majorana fermions subjected to a parity constraint), we naturally get back Kitaev's honeycomb model [38]. Similar constructions with two η's and four χ's per site on the square [40] and diamond [39] lattices would also lead to exactly solved spin liquid models, as we demonstrate in detail in Appendix D. With the same logic, it is possible to construct spin liquid models on more general lattices, and we leave this as an interesting future direction.

Note added. Recently, a related paper appeared [45]. Part of the present work overlaps with Ref. [45] in that both discuss how existing methods for bosonizing spinless fermions can be naturally generalized to cover multiple fermion flavors per site.

ACKNOWLEDGMENTS

This work is partially supported by the RGC through Grant No. 26308021.

APPENDIX A: RELATIONS BETWEEN SO(8) REPRESENTATIONS

In our $\eta\chi$ formalism of square lattice, the qubit representation forms a spinor representation for SO(8) or, say, Spin(8). In Ref. [31] the qubit representation is also constructed using auxiliary Majorana fermions. We show that the two ways are physically equivalent. There are some subtle issues about finding a transformation of Clifford basis η, χ to $\eta^1, \ldots, \eta^8$ in the Appendix of Ref. [31], since Clifford algebra intrinsically lives on the 16-dimensional Hilbert space, while in the case of spin-charge separation, the physical meaning of Γ_+ subspace is vague. But restricting to Γ_- subspace, we can take a simpler way to look for local unitary transformations of qubit representations of operators, such that Λ's can be mapped to their expressions in Ref. [31] correspondingly. Without ambiguity, we may abuse the notation of indices i, j, α, x.

We first review some basic facts of the SO(8) group [46]. It is a simple Lie group of rank 4. In terms of orthonormal basis vector $\boldsymbol{e}^i$ the four simple roots are $\boldsymbol{\alpha}^1 = \boldsymbol{e}^1 - \boldsymbol{e}^2, \boldsymbol{\alpha}^2 = \boldsymbol{e}^2 - \boldsymbol{e}^3$, $\boldsymbol{\alpha}^3 = \boldsymbol{e}^3 - \boldsymbol{e}^4$, and $\boldsymbol{\alpha}^4 = \boldsymbol{e}^3 + \boldsymbol{e}^4$. Its fundamental weights in the same basis are

$$\begin{aligned} &\mu^1 = (1, 0, 0, 0), \quad \mu^2 = (1, 1, 0, 0), \\ &\mu^3 = \tfrac{1}{2}(1, 1, 1, -1), \quad \mu^4 = \tfrac{1}{2}(1, 1, 1, 1). \end{aligned} \tag{A1}$$

All inequivalent irreducible representations can be constructed from highest weight states $|\mu\rangle$, $\mu = m^i\mu^i$ with $m^i \in \mathbb{N}$. Fundamental representation $|\mu^1\rangle$ is vector representation, denoted as $\mathbf{8}_v$. $|\mu^3\rangle$ and $|\mu^4\rangle$ are two spinor representations corresponding to different parity, denoted as $\mathbf{8}_{s^-}$ and $\mathbf{8}_{s^+}$, respectively.

In the $\eta\chi$ formalism, the generators $\boldsymbol{H} = (H_1, H_2, H_3, H_4)$ of Cartan subalgebra are chosen from θ and ϕ in Eq. (8) (for

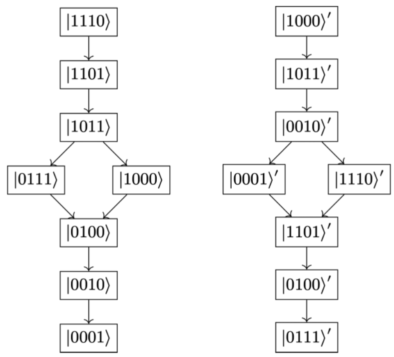

FIG. 7. Weight diagrams of two irreps.

convenience we replace $n_{a,b,d,g}$ by $n_{1,2,3,4}$, respectively):

$$H_1 = -\theta^{12} = \tfrac{1}{2}(2n_1 - 1), \quad H_2 = -\theta^{34} = \tfrac{1}{2}(2n_2 - 1),$$
$$H_3 = \phi^{12} = \tfrac{1}{2}(2n_3 - 1), \quad H_4 = \phi^{34} = \tfrac{1}{2}(2n_4 - 1). \tag{A2}$$

Then irreducible representation (irrep) $\mathbf{8}_{s^-}$ has the highest weight state $|1110\rangle$.

Although it is not obvious how to find a local unitary operator by η's and χ's such that our formalism here can be turned into ones of spin-charge separation in Ref. [31], we can first consider local unitary transformations between qubit representations. We look for a unitary matrix U such that

$$U\Lambda^{ij}U^{-1} = \Lambda^{ij}_{sc}, \tag{A3}$$

where Λ_{sc} means the corresponding expression in Eq. (112) of Ref. [31]. When $\rho = -1$, this 8×8 matrix U turns out to be

$$U = \begin{pmatrix} 0 & 0 & 0 & X \\ 0 & 0 & -iX & 0 \\ X & 0 & 0 & 0 \\ 0 & -iX & 0 & 0 \end{pmatrix}, \tag{A4}$$

where X is a 2×2 Pauli matrix, and each entry denotes a 2×2 block. Under this transformation, the generators in Eq. (A2) are mapped to another form. We can readily check that the states after being mapped by U still form an $\mathbf{8}_{s^-}$ irrep. More explicitly, for a state with weight $|\mu^i\rangle$ in the $\eta\chi$ qubit representation, if we operate with transformed Cartan generators on these states,

$$UH_\alpha U^{-1} \cdot U|\mu^i\rangle = \mu^i_\alpha U|\mu^i\rangle, \quad \alpha \in \{1, 2, 3, 4\}, \tag{A5}$$

which means $|\mu^i\rangle$ still has weight μ^i. We have summarized the weight diagram of states in the $\eta\chi$ qubit representation and the transformed qubit representation. Notice that in Ref. [31] spin representations are defined from particle number representations in a different way from ours.

After unitary transformation the irrep $\mathbf{8}_{s^-}$ has the highest weight state $|1000\rangle'$ (we use $'$ to distinguish states in the sense of spin-charge separation). Notice in Ref. [31] the particle number is $n = 1 + n_c - n_h$, and z-component spin is $S^z = \frac{1}{2}(n_u - n_d)$. So $|1000\rangle'$ represents a state $n = 2, S^z = 0$, which is the same as $|1110\rangle$ in the $\eta\chi$ formalism (if we ignore the auxiliary degrees of freedom). Similarly one may compare all descendants in the two irreps as shown in Fig. 7.

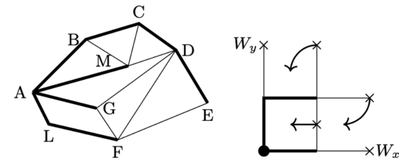

FIG. 8. A planar graph with some vertices and edges. The thick lines constitute a maximal tree T, and every edge not belonging to T generates a homology class, namely, a 1-cycle. The number of generators is equal to the number of "holes" (Euler characteristic).

APPENDIX B: GENERATORS OF $H_1(X, \mathbb{Z})$ OF CONNECTED GRAPHS

In this Appendix we discuss how to find generators of the first homology group for a connected graph. For example, Fig. 8 is a planar graph that consists of 9 vertices and 15 edges. A maximal tree T is emphasized by thick lines. Then for every edge $e \notin T$, adding it to this maximal tree will produce a class of cycle, like adding the edge BM to T will produce a cycle ABM. In the language of bosonization, each cycle on the fermionic side is an identity, while mapping to the bosonic side gives a constraint. In Fig. 8 there are seven edges not included in T and they generate the whole $H_1(X, \mathbb{Z}) \cong \mathbb{Z}^7$.

For a nonplanar connected graph, for instance, a lattice with periodic boundary conditions, the counting of generators of $H_1(X, \mathbb{Z})$ is also similar, but the counting of independent "holes" is not as obvious as in the planar case. In a generic situation, we can start from one vertex of the graph and find a maximal tree, count edges not included in the tree, and assign each of them with a cycle.

We start from an example of a 2×2 square lattice. In Fig. 8 the dangling edges with crosses ("crossed edge") are linking to periodic sites respectively. The maximal tree is stressed with thick lines. The left-most crossed edge gives the Wilson loop constraint along the y direction, and the bottom crossed edge gives the Wilson loop constraint along the x direction. The right edge of the square gives a plaquette to its left. The

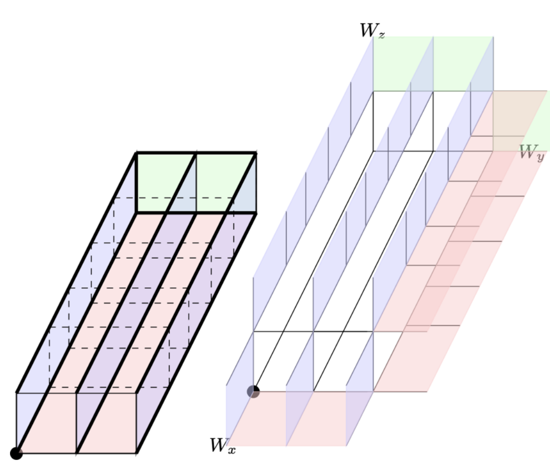

FIG. 9. Plaquette constraints for cubic lattice on 3-torus. The left figure shows independent plaquettes colored in cuboid (for vision the upper surface is not exhibited). The right figure shows Wilson loops and extra plaquettes from periodic boundary conditions.

two crossed edges at the top-right corner give two plaquettes to their left and right.

Now we consider a cubic lattice. To make it concrete we set $L_x = 6$, $L_y = 3$, $L_z = 2$. We first consider the $(L_x - 1) \times (L_y - 1) \times (L_z - 1)$ cuboid; its maximal tree is chosen to be double layers of "E" shape with an extra edge connecting two layers. Using edges in this cuboid we can get plaquettes living on five surfaces of the cuboid. We use different colors to shade the plaquette constraints from those edges; these surfaces include $(y = 0, xz)$, $(y = 2, xz)$, $(x = 0, yz)$, $(z = 0, xy)$, and $(z = 1, xy)$ (see Fig. 9). Then we turn to those dangling edges. The strategy is as follows. First determine the Wilson loop constraints, and then assign each dangling edge to a plaquette on the extension of cuboid surfaces. This strategy makes Wilson loops move freely in the whole graph, and plaquette constraints are all independent and easy to count.

The counting of plaquettes is straightforward. Combining these contributions, we have

$$\begin{aligned}\#\{\text{constraints}\} &= (L_xL_z - 1)L_y + (L_y - 1)(L_x - 1)L_z \\ &\quad + (L_x - 1)L_z + (L_yL_z - 1) + (L_y - 1) + 3 \\ &= 2L_xL_yL_z + 1.\end{aligned}$$

The last line is exactly the same as the exponent of the denominator in Eq. (13).

APPENDIX C: ROTATION MATRICES AND EXPONENTIAL MAPS

In this section we list some useful equations of rotation matrices of cubic lattice for all types of axes. As the notation in main text, we denote a 6×6 rotation matrix as R, for $\mathbf{\Lambda}^T \Rightarrow \mathbf{\Lambda}^T R$, and its exponential form $R = e^{-2A}$ where A is a 6×6 antisymmetric real matrix. We summarize some equations of exponential maps so that one can readily write down the corresponding unitary operator of rotation.

For fourfold axes we just use the V_{C_4} of a square lattice to write down similar operators in the cubic lattice:

$$V_{[0,0,1]} = e^{-i\frac{\pi}{4}\sum_r\left(\phi_r^{12}+\phi_r^{34}-\sqrt{2}\left(\phi_r^{13}+\phi_r^{24}+\phi_r^{14}-\phi_r^{23}\right)\right)}, \tag{C1a}$$

$$V_{[1,0,0]} = e^{-i\frac{\pi}{4}\sum_r\left(\phi_r^{56}+\phi_r^{12}-\sqrt{2}\left(\phi_r^{51}+\phi_r^{62}+\phi_r^{52}-\phi_r^{61}\right)\right)}, \tag{C1b}$$

$$V_{[0,-1,0]} = e^{-i\frac{\pi}{4}\sum_r\left(\phi_r^{56}+\phi_r^{34}-\sqrt{2}\left(\phi_r^{53}+\phi_r^{64}+\phi_r^{54}-\phi_r^{63}\right)\right)}. \tag{C1c}$$

For twofold axes:

$$[1,1,0]: R = \begin{pmatrix} 0&0&1&0&0&0\\ 0&0&0&1&0&0\\ 1&0&0&0&0&0\\ 0&1&0&0&0&0\\ 0&0&0&0&0&1\\ 0&0&0&0&-1&0 \end{pmatrix} = \exp\left[-\frac{\pi}{2}\begin{pmatrix} 0&1&0&-1&0&0\\ -1&0&1&0&0&0\\ 0&-1&0&1&0&0\\ 1&0&-1&0&0&0\\ 0&0&0&0&0&-1\\ 0&0&0&0&1&0 \end{pmatrix}\right], \tag{C2}$$

$$[1,-1,0]: R = \begin{pmatrix} 0&0&0&1&0&0\\ 0&0&-1&0&0&0\\ 0&1&0&0&0&0\\ -1&0&0&0&0&0\\ 0&0&0&0&0&1\\ 0&0&0&0&-1&0 \end{pmatrix} = \exp\left[-\frac{\pi}{2}\begin{pmatrix} 0&0&0&-1&0&0\\ 0&0&1&0&0&0\\ 0&-1&0&0&0&0\\ 1&0&0&0&0&0\\ 0&0&0&0&0&-1\\ 0&0&0&0&1&0 \end{pmatrix}\right], \tag{C3}$$

$$[1,0,1]: \quad R = \begin{pmatrix} 0&0&0&0&1&0\\ 0&0&0&0&0&1\\ 0&0&0&-1&0&0\\ 0&0&1&0&0&0\\ 1&0&0&0&0&0\\ 0&1&0&0&0&0 \end{pmatrix} = \exp\left[-\frac{\pi}{2}\begin{pmatrix} 0&1&0&0&0&-1\\ -1&0&0&0&1&0\\ 0&0&0&1&0&0\\ 1&0&-1&0&0&0\\ 0&-1&0&0&0&1\\ 1&0&0&0&-1&0 \end{pmatrix}\right], \tag{C4}$$

$$[-1,0,1]: \quad R = \begin{pmatrix} 0&0&0&0&0&1\\ 0&0&0&0&-1&0\\ 0&0&0&-1&0&0\\ 0&0&1&0&0&0\\ 0&1&0&0&0&0\\ -1&0&0&0&0&0 \end{pmatrix} = \exp\left[-\frac{\pi}{2}\begin{pmatrix} 0&0&0&0&0&-1\\ 0&0&0&0&1&0\\ 0&0&0&1&0&0\\ 0&0&-1&0&0&0\\ 0&-1&0&0&0&0\\ 1&0&0&0&0&0 \end{pmatrix}\right], \tag{C5}$$

$$[0,1,1]: \quad R = \begin{pmatrix} 0&-1&0&0&0&0\\ 1&0&0&0&0&0\\ 0&0&0&0&1&0\\ 0&0&0&0&0&1\\ 0&0&1&0&0&0\\ 0&0&0&1&0&0 \end{pmatrix} = \exp\left[-\frac{\pi}{2}\begin{pmatrix} 0&1&0&0&0&0\\ -1&0&0&0&0&0\\ 0&0&0&1&0&-1\\ 0&0&-1&0&1&0\\ 0&0&0&-1&0&1\\ 0&0&1&0&-1&0 \end{pmatrix}\right], \tag{C6}$$

$$[0,-1,1]: \quad R=\begin{pmatrix}0&-1&0&0&0&0\\1&0&0&0&0&0\\0&0&0&0&0&1\\0&0&0&0&-1&0\\0&0&0&1&0&0\\0&0&-1&0&0&0\end{pmatrix} = \exp\left[-\frac{\pi}{2}\begin{pmatrix}0&1&0&0&0&0\\-1&0&0&0&0&0\\0&0&0&0&0&-1\\0&0&0&0&1&0\\0&0&0&-1&0&0\\0&0&1&0&0&0\end{pmatrix}\right]. \tag{C7}$$

For threefold axes:

$$[1,1,1]: \quad R=\begin{pmatrix}0&0&1&0&0&0\\0&0&0&1&0&0\\0&0&0&0&1&0\\0&0&0&0&0&1\\1&0&0&0&0&0\\0&1&0&0&0&0\end{pmatrix} = \exp\left[\frac{2\pi}{3\sqrt{3}}\begin{pmatrix}0&0&1&0&-1&0\\0&0&0&1&0&-1\\-1&0&0&0&1&0\\0&-1&0&0&0&1\\1&0&-1&0&0&0\\0&1&0&-1&0&0\end{pmatrix}\right], \tag{C8}$$

$$[1,-1,1]: \quad R=\begin{pmatrix}0&0&0&0&0&-1\\0&0&0&0&1&0\\0&1&0&0&0&0\\-1&0&0&0&0&0\\0&0&1&0&0&0\\0&0&0&1&0&0\end{pmatrix} = \exp\left[\frac{2\pi}{3\sqrt{3}}\begin{pmatrix}0&0&0&1&0&-1\\0&0&-1&0&1&0\\0&1&0&0&-1&0\\-1&0&0&0&0&-1\\0&-1&1&0&0&0\\1&0&0&1&0&0\end{pmatrix}\right], \tag{C9}$$

$$[-1,-1,1]: \quad R=\begin{pmatrix}0&0&1&0&0&0\\0&0&0&1&0&0\\0&0&0&0&0&-1\\0&0&0&0&1&0\\0&1&0&0&0&0\\-1&0&0&0&0&0\end{pmatrix} = \exp\left[\frac{2\pi}{3\sqrt{3}}\begin{pmatrix}0&0&1&0&0&1\\0&0&0&1&-1&0\\-1&0&0&0&0&-1\\0&-1&0&0&1&0\\0&1&0&-1&0&0\\-1&0&1&0&0&0\end{pmatrix}\right], \tag{C10}$$

$$[-1,1,1]: \quad R=\begin{pmatrix}0&0&0&0&1&0\\0&0&0&0&0&1\\0&1&0&0&0&0\\-1&0&0&0&0&0\\0&0&0&-1&0&0\\0&0&1&0&0&0\end{pmatrix} = \exp\left[\frac{2\pi}{3\sqrt{3}}\begin{pmatrix}0&0&0&1&1&0\\0&0&-1&0&0&1\\0&1&0&0&0&-1\\-1&0&0&0&1&0\\-1&0&0&-1&0&0\\0&-1&1&0&0&0\end{pmatrix}\right]. \tag{C11}$$

APPENDIX D: CONNECTION TO SPIN LIQUID MODELS

We consider a diamond lattice. There are two sets of sublattices, and each vertex has four types of links to its nearest neighbors. Each vertex can be assigned a tetrahedron, whose four vertices correspond to χ^i, $i \in \{1,2,3,4\}$, labeled as in Fig. 10. We label the two $\chi^{i'}$s on the same edge with the same number, so the number can be regarded as assigned to the edge. The four types of edges are denoted by $\mu(e) = 1, 2, 3, 4$. Besides, there are another two Majorana fermions η^1, η^2 on each site. The representation we choose is as follows:

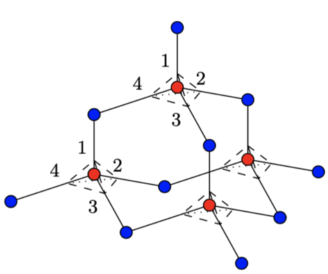

FIG. 10. Ryu's model on a diamond lattice. The figure shows two types of sites in the diamond lattice with red A type and blue B type. Numbers label the edge to which a pair of $\chi^{i'}$s is attached. Each site has a tetrahedron. Tetrahedrons of blue sites are not shown in the figure.

$$\begin{aligned}&\Phi^{12} = X^{(1)},\ \Phi^{23} = Z^{(1)},\ \Phi^{13} = Y^{(1)},\\ &\Phi^{41} = Z^{(1)}Y^{(2)},\ \Phi^{42} = -Y^{(1)}Y^{(2)},\ \Phi^{43} = X^{(1)}Y^{(2)}.\end{aligned} \tag{D1}$$

Representation for $\Lambda^{\alpha x} = i\eta^{\alpha}\chi^{x}$ is chosen as

$$\begin{aligned}&\Lambda^{11} = Z^{(1)}X^{(2)},\ \Lambda^{12} = -Y^{(1)}X^{(2)},\\ &\Lambda^{13} = X^{(1)}X^{(2)},\ \Lambda^{14} = Z^{(2)},\\ &\Lambda^{21} = Z^{(1)}Z^{(2)},\ \Lambda^{22} = -Y^{(1)}Z^{(2)},\\ &\Lambda^{23} = X^{(1)}Z^{(2)},\ \Lambda^{24} = X^{(2)}.\end{aligned} \tag{D2}$$

We use $\mu(e)$, $s(e)$, and $t(e)$ to denote edge type, red site, and blue site of an edge e, with mapping arrows from red sites to blue sites. With such a qubit representation, a Hamiltonian $H = \sum_e J_{\mu(e)}(i\gamma^1_{s(e)}\gamma^1_{(t)} + i\gamma^2_{s(e)}\gamma^2_{t(e)})$ on the fermionic side is mapped to

$$\begin{aligned}H &= -\sum_e J_{\mu(e)}\Lambda^{1\mu(e)}_{s(e)}\Lambda^{1\mu(e)}_{t(e)}\\ &= -\sum_e J_{\mu(e)}\sigma^{\mu(e)}_{s(e)}\sigma^{\mu(e)}_{t(e)}\big(X^{(2)}_{s(e)}X^{(2)}_{t(e)} + Z^{(2)}_{s(e)}Z^{(2)}_{t(e)}\big),\end{aligned} \tag{D3}$$

which is Ryu's diamond model [39]. This is an example of 3D quantum spin liquid model. Both Hamiltonians of Ryu's diamond model and Kitaev's honeycomb model pick up the unique ground state satisfying the plaquette constraints so there is no need to include constraints in the Hamiltonians, according to Lieb's theorem [47]. These plaquette terms appear as effective theories automatically in the strong-coupling limit. In fact, the same Hamiltonian can be constructed for a square lattice with two types of sites interspersed. Interested readers are referred to Ref. [40].

[1] P. Jordan and E. Wigner, Über das paulische äquivalenzverbot, Z. Phys. **47**, 631 (1928).
[2] J. Wosiek, A local representation for fermions on a lattice, Acta Phys. Pol. B **13**, 543 (1982).
[3] A. M. Szczerba, Spins and fermions on arbitrary lattices, Commun. Math. Phys. **98**, 513 (1985).
[4] E. Fradkin, Jordan-Wigner Transformation for Quantum-Spin Systems in Two Dimensions and Fractional Statistics, Phys. Rev. Lett. **63**, 322 (1989).
[5] Y. R. Wang, Ground state of the two-dimensional antiferromagnetic heisenberg model studied using an extended Wigner-Jordan transformation, Phys. Rev. B **43**, 3786 (1991).
[6] Z. Weng, D. Sheng, and C. Ting, Understanding high-T_c cuprates based on the phase string theory of doped antiferromagnet, Physica C **341–348**, 67 (2000).
[7] R. C. Ball, Fermions without Fermion Fields, Phys. Rev. Lett. **95**, 176407 (2005).
[8] L. Huerta and J. Zanelli, Bose-Fermi Transformation in Three-Dimensional Space, Phys. Rev. Lett. **71**, 3622 (1993).
[9] F. Verstraete and J. I. Cirac, Mapping local Hamiltonians of fermions to local Hamiltonians of spins, J. Stat. Mech.: Theory Exp. (2005) P09012.
[10] H.-D. Chen, C. Fang, J. Hu, and H. Yao, Quantum phase transition in the quantum compass model, Phys. Rev. B **75**, 144401 (2007).
[11] X.-Y. Feng, G.-M. Zhang, and T. Xiang, Topological Characterization of Quantum Phase Transitions in a Spin-1/2 Model, Phys. Rev. Lett. **98**, 087204 (2007).
[12] H.-D. Chen and J. Hu, Exact mapping between classical and topological orders in two-dimensional spin systems, Phys. Rev. B **76**, 193101 (2007).
[13] H.-D. Chen and Z. Nussinov, Exact results of the Kitaev model on a hexagonal lattice: Spin states, string and brane correlators, and anyonic excitations, J. Phys. A: Math. Theor. **41**, 075001 (2008).
[14] E. Cobanera, G. Ortiz, and Z. Nussinov, The bond-algebraic approach to dualities, Adv. Phys. **60**, 679 (2011).
[15] Z. Nussinov, G. Ortiz, and E. Cobanera, Arbitrary dimensional Majorana dualities and architectures for topological matter, Phys. Rev. B **86**, 085415 (2012).
[16] E. Zohar and J. I. Cirac, Eliminating fermionic matter fields in lattice gauge theories, Phys. Rev. B **98**, 075119 (2018).
[17] K. Minami, Solvable Hamiltonians and fermionization transformations obtained from operators satisfying specific commutation relations, J. Phys. Soc. Jpn. **85**, 024003 (2016).
[18] K. Minami, Honeycomb lattice Kitaev model with Wen–toric-code interactions, and anyon excitations, Nucl. Phys. B **939**, 465 (2019).
[19] M. Ogura, Y. Imamura, N. Kameyama, K. Minami, and M. Sato, Geometric criterion for solvability of lattice spin systems, Phys. Rev. B **102**, 245118 (2020).
[20] Y.-A. Chen, A. Kapustin, and D. Radičević, Exact bosonization in two spatial dimensions and a new class of lattice gauge theories, Ann. Phys. **393**, 234 (2018).
[21] Y.-A. Chen and A. Kapustin, Bosonization in three spatial dimensions and a 2-form gauge theory, Phys. Rev. B **100**, 245127 (2019).
[22] Y.-A. Chen, Exact bosonization in arbitrary dimensions, Phys. Rev. Research **2**, 033527 (2020).
[23] A. Bochniak, B. Ruba, J. Wosiek, and A. Wyrzykowski, Constraints of kinematic bosonization in two and higher dimensions, Phys. Rev. D **102**, 114502 (2020).
[24] A. Bochniak and B. Ruba, Bosonization based on Clifford algebras and its gauge theoretic interpretation, J. High Energy Phys. 12 (2020) 118.
[25] S. B. Bravyi and A. Y. Kitaev, Fermionic quantum computation, Ann. Phys. **298**, 210 (2002).
[26] J. T. Seeley, M. J. Richard, and P. J. Love, The Bravyi-Kitaev transformation for quantum computation of electronic structure, J. Chem. Phys. **137**, 224109 (2012).
[27] K. Setia and J. D. Whitfield, Bravyi-Kitaev superfast simulation of electronic structure on a quantum computer, J. Chem. Phys. **148**, 164104 (2018).
[28] K. Setia, S. Bravyi, A. Mezzacapo, and J. D. Whitfield, Superfast encodings for fermionic quantum simulation, Phys. Rev. Research **1**, 033033 (2019).
[29] C. Derby, J. Klassen, J. Bausch, and T. Cubitt, Compact fermion to qubit mappings, Phys. Rev. B **104**, 035118 (2021).
[30] C. Derby and J. Klassen, A compact fermion to qubit mapping part 2: Alternative lattice geometries, arXiv:2101.10735
[31] H. C. Po, Symmetric Jordan-Wigner transformation in higher dimensions, arXiv:2107.10842.
[32] G. Li, A. Luican, J. M. B. Lopes Dos Santos, A. H. Castro Neto, A. Reina, J. Kong, and E. Y. Andrei, Observation of Van Hove singularities in twisted graphene layers, Nat. Phys. **6**, 109 (2010).
[33] R. Bistritzer and A. H. MacDonald, Moiré bands in twisted double-layer graphene, Proc. Natl. Acad. Sci. USA **108**, 12233 (2011).
[34] D. Wong, Y. Wang, J. Jung, S. Pezzini, A. M. DaSilva, H.-Z. Tsai, H. S. Jung, R. Khajeh, Y. Kim, J. Lee, S. Kahn, S. Tollabimazraehno, H. Rasool, K. Watanabe, T. Taniguchi, A. Zettl, S. Adam, A. H. MacDonald, and M. F. Crommie, Local spectroscopy of moiré-induced electronic structure in gate-tunable twisted bilayer graphene, Phys. Rev. B **92**, 155409 (2015).
[35] Y. Cao, V. Fatemi, A. Demir, S. Fang, S. L. Tomarken, J. Y. Luo, J. D. Sanchez-Yamagishi, K. Watanabe, T. Taniguchi,

E. Kaxiras *et al.*, Correlated insulator behaviour at half-filling in magic-angle graphene superlattices, Nature (London) **556**, 80 (2018).

[36] Y. Cao, V. Fatemi, S. Fang, K. Watanabe, T. Taniguchi, E. Kaxiras, and P. Jarillo-Herrero, Unconventional superconductivity in magic-angle graphene superlattices, Nature (London) **556**, 43 (2018).

[37] K. Kim, A. DaSilva, S. Huang, B. Fallahazad, S. Larentis, T. Taniguchi, K. Watanabe, B. J. LeRoy, A. H. MacDonald, and E. Tutuc, Tunable moiré bands and strong correlations in small-twist-angle bilayer graphene, Proc. Natl. Acad. Sci. USA **114**, 3364 (2017).

[38] A. Kitaev, Anyons in an exactly solved model and beyond, Ann. Phys. **321**, 2 (2006), January Special Issue.

[39] S. Ryu, Three-dimensional topological phase on the diamond lattice, Phys. Rev. B **79**, 075124 (2009).

[40] R. Nakai, S. Ryu, and A. Furusaki, Time-reversal symmetric Kitaev model and topological superconductor in two dimensions, Phys. Rev. B **85**, 155119 (2012).

[41] T. Sunada, Homology groups of graphs, in *Topological Crystallography: With a View Towards Discrete Geometric Analysis* (Springer Japan, Tokyo, 2013), pp. 37–51.

[42] This equality comes from the fact that a tree can be obtained by joining $|E(T)|$ disconnected edges for $|E(T)|-1$ times. Each time one vertex is resolved into the tree. So $|V(T)| = 2|E(T)| - (|E(T)-1|) = |E(T)|+1$. For a maximal tree $|V(T)| = |V(X)|$ so we get the equality.

[43] X.-G. Wen, Quantum Orders in an Exact Soluble Model, Phys. Rev. Lett. **90**, 016803 (2003).

[44] A. Kitaev, Fault-tolerant quantum computation by anyons, Ann. Phys. **303**, 2 (2003).

[45] A. Bochniak, B. Ruba, and J. Wosiek, Bosonization of Majorana modes and edge states, Phys. Rev. B **105**, 155105 (2022).

[46] H. Georgi, *Lie Algebras in Particle Physics: From Isospin to Unified Theories* (Taylor & Francis, Philadelphia, 2000).

[47] E. H. Lieb, Flux Phase of the Half-Filled Band, Phys. Rev. Lett. **73**, 2158 (1994).